AD-A115 634 FOREIGN TECHNOLOGY DIV WRIGHT-PATTERSON AFB OH F/G 20/4
ACTA MECHANICA SINICA (SELECTED ARTICLES),(U)
MAY 82 L GUOCAN, Y XIEYUAN
UNCLASSIFIED FTD-ID(RS)T-0181-82 NL

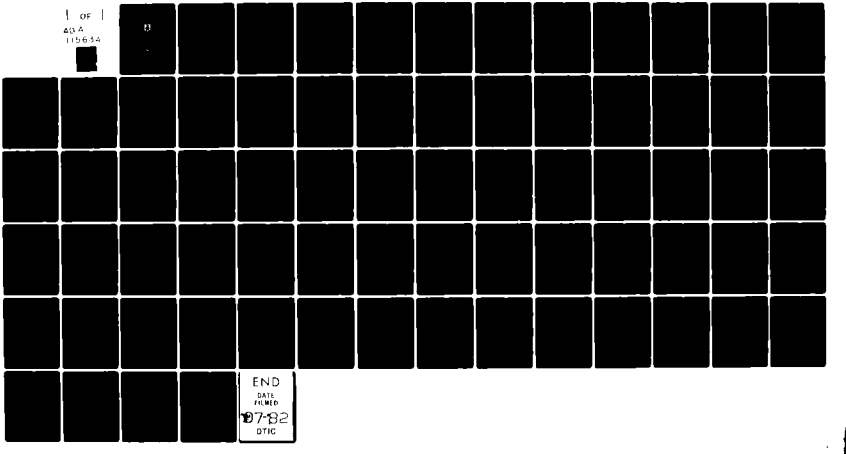

FTD-ID(RS)T-0181-82

FOREIGN TECHNOLOGY DIVISION

ACTA MECHANICA SINICA

(Selected Articles)

JUN 16 1982

A

Approved for public release;
distribution unlimited.

EDITED TRANSLATION

FTD-ID(RS)T-0181-82 17 May 1982

MICROFICHE NR: FTD-82-C-000654

ACTA MECHANICA SINICA (Selected Articles)

English pages: 68

Source: Acta Mechanica Sinica, Nr. 2, 1981,
pp. 109-135; 181-186; 194-198

Country of origin: China
Translated by: LEO KANNER ASSOCIATES
F33657-81-D-0264
Requester: FTD/TQTA

PREPARED BY:

TRANSLATION DIVISION
FOREIGN TECHNOLOGY DIVISION
WP-AFB, OHIO.

Table of Contents

GRAPHICS DISCLAIMER

All figures, graphics, tables, equations, etc. merged into this translation were extracted from the best quality copy available.

EARLY STAGES OF UNSTEADY FLOW AROUND A CYLINDER AT HIGH REYNOLDS NUMBER AND UNDER LAMINAR CONDITIONS

Ling Guocan, and Yin Xieyuan

Institute of Mechanics, Chinese Academy of Sciences (Ling), and China University of Science and Technology (Yin)

Submitted 15 May 1980

In this paper, the early stages of unsteady flow around a cylinder, started abruptly from rest and subsequently moving with a constant velocity perpendicular to its axis, are studied by coupling discrete vortex potential flow theory with boundary layer theory. The flow is considered to be laminar and incompressible, and the Reynolds number is high. The development in time of vortex motion, characteristics of flow field, boundary layer separation point and drag coefficient are given in detail. Results of coupled calculation contain the interactions between boundary layer, external potential flow field and near wake. The calculated development of symmetric vortex possesses many of the observed features in flow field visualization. Pressure and velocity distributions are also given. The drag coefficient obtained is in excellent agreement with experiment. In the calculation of boundary layer separation point, the Startford method is applied to the quasi-steady boundary layer state. The calculated result is better than those given by others and the computation is simpler. Shedding times and locations of discrete vortices, which have been generated before the boundary layer reaches the quasi-steady state, are determined according to the unsteady M. R. S. criterion. The effect of these initial discrete vortices on the main vortex development and flow field is also discussed.

Foreword

Under the laminar flow conditions of a high Reynolds number, studies of two-dimensional unsteady motion around a cylinder (started abruptly from rest and subsequently moving with a constant velocity) are important theoretically and have wide applications. In applications, when a missile moves at a large angle of attack, the characteristics of the discrete vortex flow field at various lateral cross-sections perpendicular to the missile body are quite similar to the two-dimensional unsteady motion started from rest around a cylinder. In computations of nonlinear aerodynamic force with a large angle of attack, these two above-mentioned motions are alike[1)]. The two-dimensional unsteady motion around a cylinder is the basis for analyzing discrete flow (at the leeward surface) characteristics of a missile body with a large angle of attack. Studies of vibrations of many tall, large industrial buildings and water conservation facilities (such as television towers, tall chimneys, and large bridges) because of flow, and studies of atmospheric circulation related to environmental contamination are also closely related to flow in this model. In the theoretical sense, in the case of high Reynolds numbers, flows in an entire unsteady process are very complex, including separation of unsteady boundary layer, formation and development of vortex, secondary vortex, secondary vortex pair, unsymmetrical motion of vortex, and formation and motion of Karman vortex streets. The theoretical analyses should simultaneously consider interactions of boundary layer, external flow, and flow near wake. Mathematically, this is a high-order nonlinear problem. The various theoretical methods at present are incapable of serving in a detailed description of the entire complex process. Boundary layer theory cannot be used to study flow in discrete regions; the existing boundary-layer solution [2-6] do not allow for the mutual influence of boundary layer and external

[1] The paper sums up two other papers, "The Divergent Vortex Model of Unsteady Motion Around a Cylinder and Study of Its Initial-stage Motion," and "The Initial Flow of Laminar Flow Unsteady Motion With High Reynolds Number Around a Cylinder." The first paper was read in May 1980 at the founding conference of the China Aeronautics Association Annual Science Conference. This persent paper is one of First Asia Fluid Dynamics Conference Papers, delivered in December 1980.

flow in an unsteady separation process. The convergent matching solution [6-10] related to the two-dimensional N-S equation is convergent only for a relatively short motion time ($v_\infty/R \leqslant 1$) at high Reynolds numbers; therefore, the solution can only reveal the initial flow variation after abrupt start.

An entirely numerical solution of N-S equation can give a detailed structure of the entire flow field, providing various approximate solutions with a standard for comparison. However, in the case of high Reynolds numbers, many difficulties exist in the unsteady-motion numerical solutions; moreover, the numerical solutions fail to clearly reveal flow variability; it is not convenient to analyze flow variations caused by different parameter variations. Thus, there have been scant results on this aspect, mainly described in the studies [11-16]. Within the range of higher Reynolds numbers, the main flow phenomenon in the separation zone near the wake is the vortex motion and vortex-surface variation. The experimental studies [17] also reveal that after an abrupt start and moving around a cylinder, viscosity has very little effect on motion and development of a vortex in the intermediate stage of the motion; the variation with time in the values of the circulation-zone characteristics is not related to the Reynolds numbers. So nonviscous flow theory can be used (with assistance from the concentrated vortex amount) to approximately represent actual flow of low-viscosity fluid. This is the potential flow model. The early-stage concentrated-vortex model [18-20] can be used to estimate drag variation of the initial-stage motion around the cylinder; however, after a longer time the drag drops rapidly, even appearing as a negative value, with irrational results of feedback by the concentrated vortex toward the vortex surface, pressure interruption on the object surface, and a force couple acting on the system composed of vortex surface and vortex pair. The report [21] combines the concentrated vortex model and the boundary layer theory, considering the interaction of unsteady boundary layer and external flow; variations of the separation points of the initial motion are obtained but the calculated drag considerably deviates from the actual result. The concentrated vortex model does not take into account the formation and variation of the vortex surface, as well as its influence on the flow. The model cannot correctly reveal the distribution and transmission of the vortex amount and the complex variability of flow in the separation zone. The convergent multivortex model improves on

the concentrated-vortex model by approximately indicating places of concentrated or continuous distributions of the flow field by many scattered point vortexes or linear vortexes. The discrete-vortex model can relatively clearly describe the flow corresponding to a longer time of motion; the required computations are much lighter than the numerical solutions of the N-S equation. This is a very advantageous feature in studying unsteady flow problems at high Reynolds numbers; these studies are mainly represented by the reports [22-31] and recently by [31] and [28]. These investigations have made certain gains in describing the overall results of long-time motion, such as the periodic variation of lift and drag, and the general forms of the Karmen vortex street. However, these past studies did not consider the time of occurrence of the initial discrete vortex (newborn vortex and subsequent discrete vortex) and the effect of position on vortex development and flow. Methods of determining newborn vortexes are random. In addition, many past studies were numerical studies, mostly with random assumptions and few analyses as to the physical regime.

In a situation of laminar flow with high Reynols numbers, the paper uses the method of combining the discrete vortex model and boundary-layer theory in studying the regime of initial-stage flow of unsteady motion around a cylinder, to describe the variation with time of boundary-layer separation points, formation and development of symmetrical vortexes and vortex surface, distribution of pressure and velocity at the object surface at different times, as well as variations of drag due to the cylinder. Solutions in the paper consider the interaction of boundary layer, external flow and flow near the wake of the separation flow. The paper uses the M. R. S. unsteady separation criterion to determine the detachment position and time of newborn vortex and subsequent discrete vortex, and to discuss the influence on vortex motion and flow of the discrete vortex produced before quasi-steady variation of the boundary layer.

Model and Method

The paper studies high-Reynolds-number, incompressible laminar flow. The main influence of viscosity is limited to a very thin boundary layer; after separation, the shearing layer is also very thin, as a thin vortex layer. The

vortex quantity comes from the continuous separation of the boundary layer and is fed by a small discrete nonviscous vortex with certain intensity and detaching continuously. Discrete vortices compose a vortex surface. The trend of motion of the discrete vortex is determined by the local potential flow field; its locus varies with time and constitutes vortex-surface motion. With the lengthening of time and continuous motion of the discrete vortex in the flow field, the number of vortexes increases continuously, thereby causing unsteady variation in the flow. From the solution of potential flow, the distribution of velocity and pressure at object surface are obtained to then calculate the separation of the boundary layer and to determine the position and intensity of newborn vortexes. The addition of newborn vortexes into the original vortex group forms a potential flow field of the next interval; this result can be used to calculate new separation points and correspondingly to determine new discrete vortexes. By these repetitions, the entire flow field is composed of a nonseparated flow around a cylinder and discrete vortexes and their mirror-image vortexes. The above-mentioned model considers the interaction of the boundary layer, external flow and flow near wake in the separation flow process.

Nonviscous Flow Field

The unsteady motion around a cylinder (started abruptly from rest and subsequently moving with a constant velocity) is equivalent to the abrupt addition of an unsteady motion (around a cylinder) to a uniform flow. This paper neglects the effect on fluid by abrupt placement of a cylinder. Except for the portions of boundary layer and the vortex nucleus, the circulation flow field can be considered as a nonviscous flow field, whose velocity potential satisfies the Laplace equation.

Definitions: dimensionless composite potential $W = \tilde{W}/RV_\infty$, velocity potential $\varphi = \tilde{\varphi}/RV_\infty$, flow function $\psi = \tilde{\psi}/RV_\infty$, circulation quantity $\Gamma = \tilde{\Gamma}/2\pi RV_\infty$, velocity $V = \tilde{V}/V_\infty$, time $t = V_\infty \tilde{t}/R_\infty$, pressure coefficient $c_p = (p - p_\infty) \Big/ \frac{1}{2}\rho V_\infty^2$, drag coefficient $c_D = D/\frac{1}{2}\rho V_\infty^2 R$, and lift coefficient $c_L = L/\frac{1}{2}\rho V_\infty^2 R$.

(∿ indicates the corresponding dimension quantity, and R and V_∞ represent, respectively, cylinder radius and velocity of incoming flow).

The forms and the flow equation and boundary condition in polar coordinates are

$$\nabla^2\varphi = 0$$
$$\left.\frac{\partial\varphi}{\partial r}\right|_{r=1} = 0 \qquad (1)$$

The composite function composed of the incoming uniform flow passing around a cylinder and N vortexes outside of the cylinder can be derived by the circle theorem [32]. In polar coordinates, the expression equation of the composite function is

$$W(z) = z + \frac{1}{z} - \sum_{n=1}^{N} i\Gamma_n \ln(z - z_n) + \sum_{n=1}^{N} i\Gamma_n \ln\left(z - \frac{1}{\bar{z}_n}\right) - \sum_{n=1}^{N} i\Gamma_n \ln z + \sum_{n=1}^{N} i\Gamma_n \ln(i^2\bar{z}_n) \qquad (2)$$

In the equation, z_n is the position of the n-th point vortex as a function of t; Γ_n is the intensity of the n-th discrete vortex; Γ_n does not vary with time after its determination, and the positive sign indicates a counterclockwise vortex. During the detachment time of separation of each discrete vortex, the potential flow field should satisfy Kelvin's theorem of conservation of vortex quantity. Hence, there should be superposed on a vortex quantity with an intensity the same (but opposite in direction) as the detaching discrete vortex on the cylindrical surface. After neglecting the integer items not related to z, the final simplification form of the composite function is

$$W(z) = z + \frac{1}{z} + \sum_{n=1}^{N} i\Gamma_n \ln \frac{z - \frac{1}{\bar{z}_n}}{z - z_n} \qquad (3)$$

The imaginary and real parts of the above equation can be used to derive the potential function and flow function as the following:

$$\varphi(r,\theta) = \frac{r^2+1}{r}\cos\theta - \sum_{n=1}^{N}\Gamma_n\theta^{**} + \sum_{n=1}^{N}\Gamma_n\theta^{*} \tag{4}$$

$$\varphi(r,\theta) = \frac{r^2-1}{r}\sin\theta + \sum_{n=1}^{N}\frac{\Gamma_n}{2}\ln\frac{R_1}{r_n^2 R_2} \tag{5}$$

The velocity of flow field under the polar coordinates is

$$V_r(r,\theta) = \frac{r^2-1}{r^2}\cos\theta + \sum_{n=1}^{N}\Gamma_n\frac{r_n\sin(\theta-\theta_n)}{R_1} - \sum_{n=1}^{N}\Gamma_n\frac{r_n\sin(\theta-\theta_n)}{R_2} \tag{6}$$

$$V_\theta(r,\theta) = -\frac{r^2+1}{r^2}\sin\theta - \sum_{n=1}^{N}\Gamma_n\frac{rr_n^2 - r_n\cos(\theta-\theta_n)}{R_1} + \sum_{n=1}^{N}\Gamma_n\frac{r - r_n\cos(\theta-\theta_n)}{R_2} \tag{7}$$

The velocity distribution at the object surface is

$$V_B(\theta) = -2\sin\theta + \sum_{n=1}^{N}\Gamma_n\frac{1-r_n^2}{1-2r_n\cos(\theta-\theta_n)+r_n^2} \tag{8}$$

In the equation,

$$\left.\begin{aligned}\theta^{**} &= \mathrm{tg}^{-1}\frac{rr_n\sin\theta - \sin\theta_n}{rr_n\cos\theta - \cos\theta_n}\\ \theta^{*} &= \mathrm{tg}^{-1}\frac{r\sin\theta - r_n\sin\theta_n}{r\cos\theta - r_n\cos\theta_n}\\ R_1 &= 1 + r^2r_n^2 - 2rr_n\cos(\theta-\theta_n)\\ R_2 &= r^2 + r_n^2 - 2rr_n\cos(\theta-\theta_n)\end{aligned}\right\} \tag{9}$$

The velocity of point-vortex motion is the velocity of the local flow field; the motion locus can be derived from a step-by-step integration of velocity. During the computation, the influence of the induced velocity by the vortex itself should not be included. The vortex of the k-th point vortex in polar coordinates should satisfy the following equations:

$$\frac{dr_k}{dt} = \frac{r_k^2 - 1}{r_k^2}\cos\theta_k + \sum_{n=1}^{k}\Gamma_n \frac{r_n \sin(\theta_k - \theta_n)}{S_1} - \sum_{n=k}^{N}\Gamma_n \frac{r_n \sin(\theta_k - \theta_n)}{S_2} \quad (10)$$

$$\frac{d\theta_k}{dt} = -\frac{r_k^2 + 1}{r_k^2}\sin\theta_k - \sum_{n=1}^{N}\Gamma_n \frac{r_k r_n^2 - r_n \cos(\theta_k - \theta_n)}{r_k S_1} + \sum_{n=k}^{k}\Gamma_n \frac{r_k - r_n \cos(\theta_k - \theta_n)}{r_k S_2} \quad (11)$$

In the equation,

$$\left.\begin{aligned} S_1 &= R_1(r_k, \theta_k, r_n, \theta_n), \quad S_2 = R_2(r_k, \theta_k, r_n, \theta_n), \\ (n &= 1, 2, \cdots, N; \quad k = 1, 2, \cdots, N) \end{aligned}\right\} \quad (12)$$

Γ_n should be determined by the vortex quantity at the separation point of the boundary layer. With the 2N differential equations mentioned above, the motion state of N point vortices can be determined.

By Lagrange integration, we find that the pressure distribution at object surface of unsteady motion (neglecting the mass force) is

$$c_p(\theta, t) = 1 - V_b^2 + 2\sum_{n=1}^{N}\Gamma_n \frac{\partial}{\partial t}(\theta_{n-1}^* - \theta_{n-1}^*) \quad (13)$$

Noticing that $dW = d\overline{W}, \frac{\partial \varphi}{\partial t} = \frac{\partial W}{\partial t} = \frac{\partial \overline{W}}{\partial t}$, on the cylindrical surface, while computing the item-by-item residual value to $\oint\left(\frac{dW}{dz}\right)^2 dz$ and $\frac{\partial}{\partial t}\oint \overline{W} d\bar{z}$, finally the pressure-difference drag and lift of the cylinder are derived:

$$c_D = -4\pi\sum_{k=1}^{N}\Gamma_k\left\{\left(1 + \frac{1}{r_k^2}\right)\frac{dr_k}{dt}\sin\theta_k + \left(r_k - \frac{1}{r_k}\right)\frac{d\theta_k}{dt}\cos\theta_k\right\} \quad (14)$$

$$c_L = 4\pi\sum_{k=1}^{k}\Gamma_k\left\{\left(1 + \frac{1}{r_k^2}\right)\frac{dr_k}{dt}\cos\theta_k - \left(r_k - \frac{1}{r_k}\right)\frac{d\theta_k}{dt}\sin\theta_k\right\} \quad (15)$$

In the equations, the definition of the composite velocity is $\frac{dW}{dz} = u - iv$.

Boundary Layer Separation and Intensity of Discrete Vortex

At high Reynolds numbers, the flow closely in contact with the surface of an object should satisfy the unsteady two-dimensional incompressible boundary layer equation and the corresponding initial-edge-value condition. The outer-edge condition of the boundary layer is the potential flow velocity at the object surface mentioned above. The solution to the internal and external layer flows should be obtained by coupling; therefore, the problem can be reduced to solving for the unsteady boundary-layer separation points.

Previously, all studies of unsteady motion around a cylinder by the discrete vortex model used the Prandtl separation criterion to determine the separation points of the boundary layer. At t=0.35 after starting flow motion around a cylinder, separation begins. First, separation points appear at the rear stationary point; however, for unsteady motion, separation does not certainly occur at τ=0 [33]. Moore-Rott-Sears proposed the M.R.S. criterion [34] for determining the boundary separation of unsteady flow. The clear meaning of "separation" indicates the distortion of boundary layer characteristics; the boundary layer becomes very thick with a singularity appearing in the solution, whether or not it is the beginning of separation bubbles or the wake. According to this criterion, generally the separation points are not on the object surface. When the unsteady motion tends to exhibit constant variation, the M.R.S. criterion is simplified into the Prandtl criterion. After an abrupt start of an unsteady motion around a cylinder, the first separation occurs at t=0.65 and the position is in the neighborhood of 40° from the rear stationary point. There are appreciable differences of the positions of separation points at the beginning of the motion during computations of the two separation criteria; after $t \geq 1$, these two criterion computations gradually approach each other. After a further longer time, there are no practical differences [35] between these two computations. If the separation and motion of discrete vortex can approximately represent vortex-quantity transmission after the separation of boundary layer, especially in studies of flow after abrupt start, separation points derived by the M.R.S. criterion should be relied on in determining the detachment time and position of the newborn vortex and the subsequent discrete vortex, so the discrete vortex model can be established

on a foundation with clearer physical meaning. Because the determination of this method of separation points involves a numerical method to determine the process of boundary-layer singularity, this paper does not repeat this complex computation. In considering the influence on flow by a discrete vortex produced not long ($t \leq 1$) after the abrupt start of the motion, the paper directly quotes the result given by the reports [35].

In investigating the variation of boundary-layer separation points, notwithstanding the incessant variation of the external flow field with time, the variation of separation points only requires a short time of approximately $t=1$ to become quasi-steady variation [28 and 31]. In this case, the corresponding separation points have moved by approximately 70° to positions in the neighborhood of the rear stationary point. Later, the boundary-layer separation can be computed in a quasi-steady state. This paper applies the Startford two-layer model method [37] for computing boundary-layer separation points to the quasi-steady boundary layer. Noting that the various physical quantities are a function of time and simultaneously considering that the extreme pressure and velocity values at the object surface during unsteady motion are possibly not at the same position, at the separation points, the following relationship should be satisfied:

$$\left.\begin{aligned} &\left[c_p'\left(x'\frac{dc_p'}{dx'}\right)^2\right]_s = 0.0104 \\ &x' = \theta - \theta_{BL} \\ &\theta_{BL} = \theta_{pmin} - \int_0^{\theta_{pmin}} \left(\frac{V_B}{V_B^*}\right)^5 d\theta \\ &c_p' = (p - p_{min}) \Big/ \frac{1}{2}\rho_\infty (V_B^*)^2 \end{aligned}\right\} \qquad (16)$$

In the equation, p_{min} is the minimum pressure, V_B^* is the object-surface external fringe velocity corresponding to the minimum-pressure point, and θ_{BL} is the starting point of the Blasius flat plate boundary layer used in the boundary-layer two-layer solution in the Stratford method, the conditions of two-equal-momentum thickness at the minimum pressure point, the boundary layer of actual flow and the imaginary flat plate boundary layer, are used to determine the starting point. The so-called coupled solution is the simultaneous solution of equation (16) and the external flow field.

The intensity of the discrete vortex is equal to the outgoing vortex flow of the boundary layer at the separation points in a time step interval. It is assumed that in a unit time, the vortex flow at the boundary-layer separation points is $\frac{\partial \Gamma}{\partial t}$; the circumferential-direction velocity in the boundary layer is v_θ, and the potential flow velocity at the separation point is V_{BS}, then

$$\frac{\partial \Gamma}{\partial t} = \frac{1}{2\pi}\left[\int_0^\delta \frac{\partial v_\theta}{\partial r} v_\theta dr\right], \tag{17}$$

$$\Gamma_s = \frac{1}{4\pi} V_{BS}^2 \Delta t \tag{18}$$

In the equations, Δt is the time step interval. The above equations indicate that no direct connection exists between the discrete-vortex intensity and the flow details in the boundary layer; the discrete-vortex intensity is only related to the potential flow velocity at the external edge of the separation point.

Brief Description of Computations and Main Results

The work in the paper includes the following aspects: the first is the application of discrete-vortex model to investigate the flow structure of unsteady initial-stage motion, i.e., the occurrence and development of the vortex and the variation of flow characteristics with time. The variation rule of the boundary layer separation point can refer to the reports [35], [28] and [11] as expressed with an empirical relationship equation, such as

$$\theta_s = 98.0 - 58.0\exp[-1.1968(t - 0.65)] \tag{19}$$

When $t \leq 1$ in the above equation, corresponding to separation points determined by using the M.R.S. criterion, computational values are derived after a longer time approaching the criterion of stress at the zero wall. The above-mentioned computations are briefly called Section A computations, and A is marked on the curve. The second aspect is the coupling solution of the initial-stage separation flow field by using the models and methods described in the paper. This part of the computations includes two situations: the first situation begins to be computed when the boundary layer variation tends to a quasi-steady-state

situation and the positions of the newborn vortexes are given by the equation (19) as they are situated at a place $\pm 70^{\circ}$ from the rear stationary point and the detachment time is $t_o=1.2$. By using equations (8)-(18) to make coupling computations, the second situation takes into account the effect on flow of the discrete vortexes produced during separation at $t<1.2$. The time when computation begins is $t_o=0.65$ and the position of the newborn vortex is situated at $\Theta^{o}=\pm 40^{\circ}$. After $t=1.2$, the flow field coupling computation is carried according to equations (8) to (18). Computations of the two corresponding situations mentioned above are called computations of sections B and C, and curves in the diagram are represented, respectively, by B and C. This paper uses the Runge-Kutta method to compute the vortex motion locus, and the Simpson integration and proportional root solution method to compute the separation point. For each time step, two discrete vortexes are added and at the same time six equations are added, not including the number of equations serving in computing the separation points. In the entire process, the length of the computation step is 0.125; for comparison, the step length of partial computation is 0.1 and 0.2. For computations of section A, when $t=3.9$ each vortex surface is composed of 27 discrete vortexes; totally, 162 equations should be simultaneously solved. The initial position of the discrete vortexes should have a distance from the cylindrical surface not greater than the thickness of the local boundary layer. For computation conveniences, refer to thickness computation of cylindrical boundary layer, by taking $r=1.05$. The closing of the newborn vortex from the separation point will move forward faster the positions of separation points. In order to reduce this effect, the paper adopts a method of delaying a step, i.e., after producing a newborn vortex for an interval of a time step, its inducing function begins to take into account.

The development variation of vortex: Fig. 1(a) to (d) describe the computation results of section A of vortex motion. With the lengthening of time and the development of separation at the corresponding boundary layer, Fig. 1 gives the formation and roll-up process of vortex surface behind the cylinder, giving the development of symmetric vortex of spiral shape. The motion trend of discrete vortexes is rational and the vortex surface is of sequential shape. The vortex surface is naturally composed of moving discrete vortexes, not requiring the

method of re-separation. The computation result in the paper is very similar to the figures and images shown by conventional experiments. In (a) through (d) of Fig. 2, the computation results of section B are shown. Compared with the results of section A, the positions of vortexes in section B are higher, positioning at the shoulder part behind the cylinder with narrower flow region, flatter vortex shape, and vortex roll not as sufficiently developed like that in section A. Hence, the different detachment time and positions of discrete vortexes at the initial stage will influence the variation of vortexes behind the cylinder. There is some randomness in handling the separation time and position of the initial vortex in the reports [21], [24], [50] and [51]. The study [30] considers that the position of the newborn vortex is not important; this view does not have a solid basis. As revealed by computation, if the shedding positions of newborn vortexes are not rational, or interruptions occur in the subsequent step length while detaching of discrete vortexes, or the velocity of forward motion of separation points varies greatly, this will induce irregular variation of shapes of vortex surface.

Figures 3 and 4 show the distribution of pressure and velocity at the object surface (with time) in the flowing process. From the figures, the flow characteristics at the cylindrical surface when $t \leq 1$ are little different from the distribution of potential flow without separation. With increase in time, because of lengthening and effect of vortexes behind the cylinder, when $t=1.4$ two new stationary points begin to appear in the rear half part of the cylindrical surface, i.e., the appearance of a very small circulation flow zone and gradually subsequently expanding; one terminal includes the rear stationary point and another terminal extends forward, gradually becoming a stabilized position. In the neighborhood of the stationary point, there is a low-pressure zone; its range is expanding, corresponding to the increase in time. The value of the low-pressure peak may exceed the minimum pressure value at the front half of the cylinder, and the maximum velocity at the object surface in the circulation flow region also may exceed the velocity of the incoming flow. The peak value of pressure and the position of the extreme velocity value do not coincide because of the unsteady effect. Figure 3 shows a computational example of a coupling computation of pressure distribution; from the figure, computations

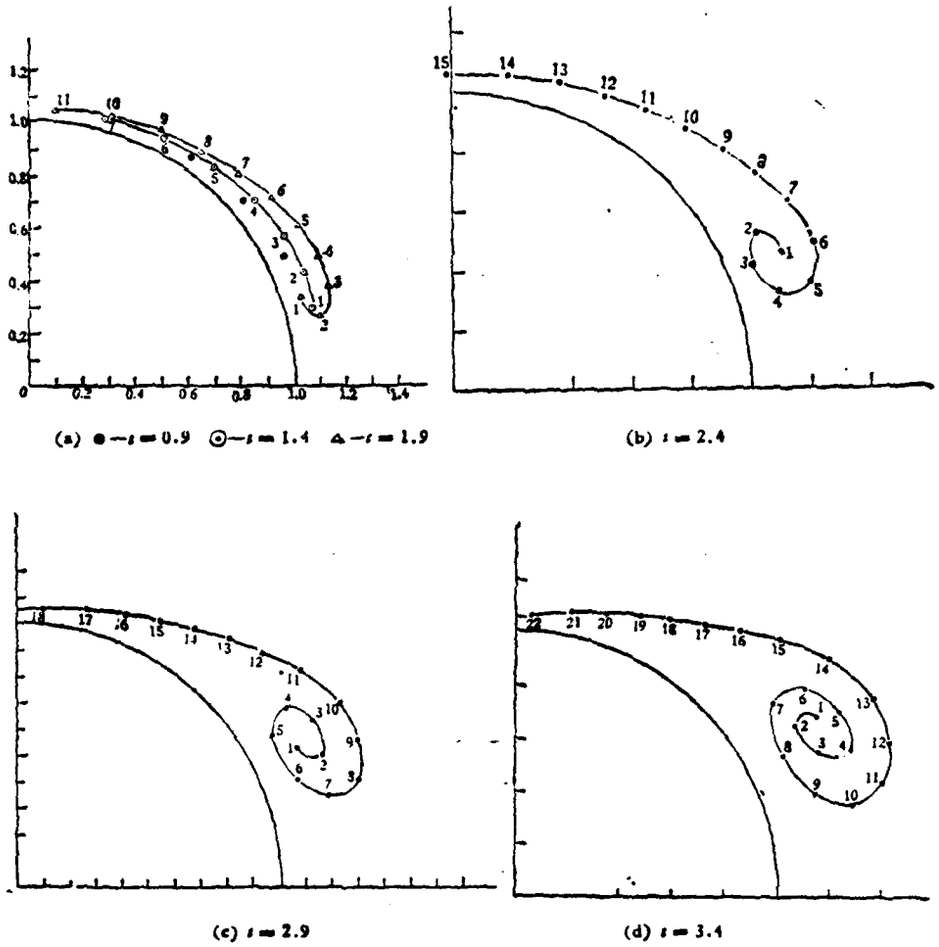

Fig. 1 (a) to (d). The formation and development of vortex (A).

at sections (B) and (C) show greater differences only in the neighborhood of the rear stationary point. This is because curve C takes into account the effect of discrete vortexes produced prior to t=1.2; in comparing curves C and A, we see that these two are relatively close. The computations reveal that when the discrete-vortex motion is irregular, and the point vortexes are very close to

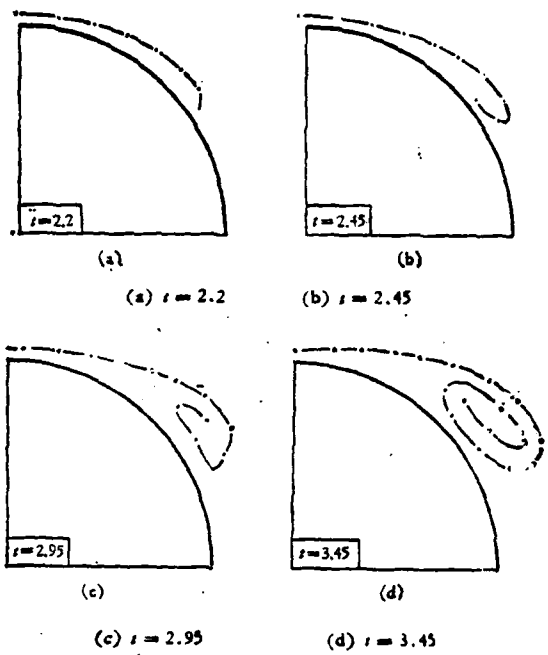

Fig. 2 (a)-(d). The formation and development of vortex (B).

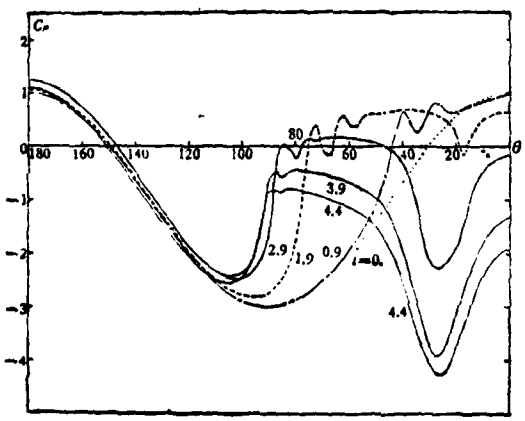

Fig. 3. Pressure distribution at object surface (A).

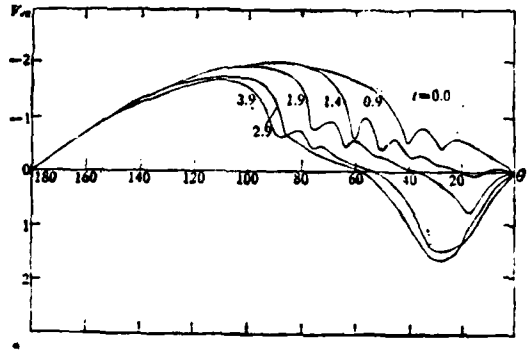

Fig. 4. Velocity distribution at object surface (A).

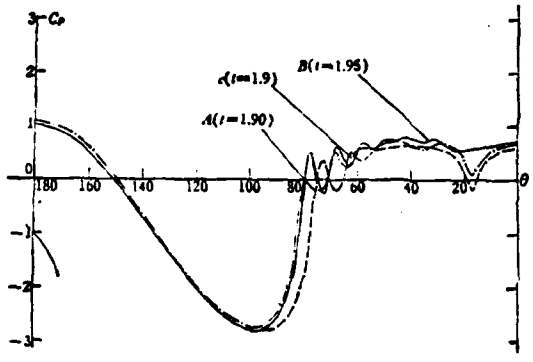

Fig. 5. Pressure distribution (B, C).

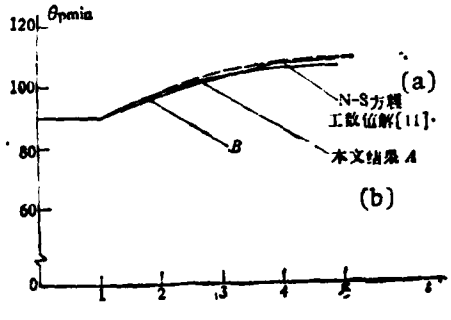

Fig. 6. Variation of minimum pressure points.
Key: (a) Numerical solution [11] of N-S equation; (b) Results of this paper A.

the object surface, computation of pressure or velocity departs from the actual cases because of the singularity effect of the induced velocity. After passing through peak value, the circulation flow along the object surface undergoes velocity reduction and pressure rise within a considerable period of time; attention should be given to the new flow phenomenon induced by the process. As for the computations mentioned above, at present there are no adequate experimental data or accurate solutions for comparison. Figure 6 gives the positions of the minimum pressure points; by comparing the computation from the figure and the numerical solution of N-S equation in manuscript [11], we see that these two are very close. The drag variations of pressure difference around the cylinder are listed in Fig. 7.

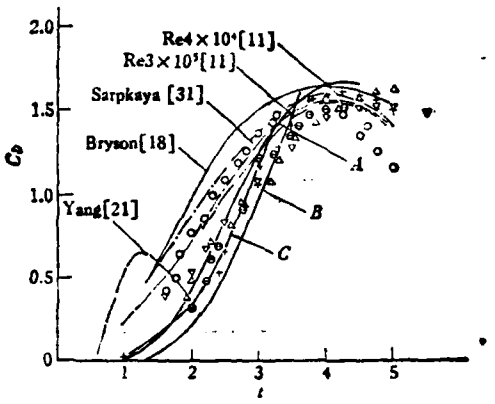

Fig. 7. Drag coefficient: ___ computations in the paper; + Rel.535·10^4 experimental value [36].

o Re 2.030×10⁴, [36], △ Re 3.200×10⁴ [36]
▽ Re 3.280×10⁴, [36], ⊖ Re 2.070×10⁴ [36]

Comparing the section (A) computations with the experiment in manuscript [36], there is a relatively good agreement. Curve B is slightly lower than the experimental values; however, when the effect of the discrete vortexes is taken into account before t≤1.2, the drag will increase and equal to the experimental result. In the figures, the computational results of the concentrated vortex model are given; the results depart considerably from the actual results. Variations of the separation points at the initial motion period are listed in Fig. 8;

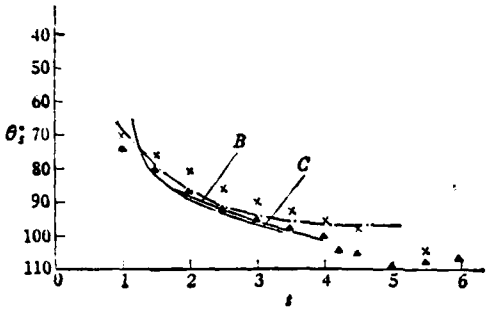

Fig. 8. Separation points of boundary layer:
___ solutions in the paper;
-·-[11] -×-×-×-[31] -▲-▲-▲-[28]

this is the result of coupling computation under mutual action of internal and external-layer flows. With increase of time, at first the separation points rapidly move forward, and then vary slowly. Computations in the paper show results in the initial stage consistent with those in [28]; however, the method is relatively simple and relatively close to the numerical solution of N-S equation in [11]. Comparing computations in the paper and the Polhausen method in [31], there is an obvious improvement; the divergent angle computed from the Polhausen method is obviously understated. At $t \leq 1.2$, the differences between the separation points, and the studies [28] and [31] are due to different separation criteria. Curve B differs only slightly from curve C; this means that the effect of the discrete vortex produced when $t<1.2$ is mainly limited to the neighborhood of the rear stationary point, having little effect on most areas around the cylinder. This is consistent with those shown in Fig. 5, the flow characteristics at an object surface.

This paper is limited to studies of the initial-period situation of separation flow; the motion time corresponding to the computations is relatively short. If computations are continued with increase in time, the separation points will slowly move forward (Fig. 8); the drag also increases with the continuous enlargement of the symmetric vortexes (as shown by curves B and C in Fig. 7). This trend

is not consistent with actuality. Actually, after the motion time is increased, the shearing layer behind the cylinder will be separated and reverse-direction vortexes are generated under the action of reverse-pressure gradient. Because the buildup and influence of the reverse-direction vortex have a bearing on distributions of pressure and velocity, as well as on the separation point and drag, the above-mentioned computations in the paper, thus far, do not include this factor, which will be discussed in another paper.

Conclusions

This paper uses a method of combining the discrete vortex model and boundary layer theory to study the unsteady initial-stage separation flow in a situation of high-Reynolds-number, incompressible laminar flow. The study derives the variation rule (with time) of vortex motion, distribution of pressure and velocity of flow field, and separation points of boundary layer and drag. The vortex buildup process obtained by computations closely resembles the diagrams plotted experimentally. Variations of the distribution of pressure and velocity of the object surface are rational; compared to available results, computations of minimum pressure points are very close. In coupling computations of separation points, the Stratford method is applied to the quasi-steady boundary layer of external flow as varying with time; the computations are simple, yielding satisfactory results. The drag computations are quite consistent with the experimental results.

The detailed investigations in the paper on flow characteristics are advantageous to the analysis of flow regime. The variations of distributions of pressure and velocity at the object surface reveal that after a short time following the circulation flow zone, the shearing layer of the motion is under the control of the reverse-pressure gradient; attention should be given to the separation of the rear shearing layer and its effect on flow.

Before the boundary layer begins its quasi-steady variations, the discrete vortexes produced by the initial separation exert effects on vortex motion behind the cylinder and on the pressure and velocity distributions in the local zone at

the object surface. Moreover, the discrete vortexes slightly increase the drag; this has little effect on the separation points. The initial positions and shedding times of these discrete vortexes should be determined from the M.R.S. separation criterion.

LITERATURE

[1] Thwaites, B. ed., Imcompressible Aerodynamics the University Press Oxford 1st ed. (1960), 411.
[2] Blasius, H. *Zeit. Math. Phys.*, 56(1908).
[3] Goldstein, S. & Rosenhead, L., *Proc Cambrige Phil. Soc.*, s 32(1936), 392—401.
[4] Watson, E. J., *Proc. Roy Soc. Ser., A*, 231(1951), 104—116.
[5] Schuh, H., Z. F. Flugwiss, 5(1953), 122—131.
[6] Wang, C. Y., *J. Math. Phys.*, 46(1967), 195—202.
[7] Wang, C. Y., *J. F. M.*, 60(1973), 105—127.
[8] Collins, W. M. & Dennis, S. C. R., *Quart. J. Mech. Appl. Math.*, 26(1973), 53—75.
[9] Collins, W. M. & Dennis, S. C. R., *J. F. M.*, 60(1973), 105—127.
[10] Bar-Lev & Yang, H. T., *J. F. M.*, 72, part 4(1975), 625—647.
[11] Thoman, D. C. & Szewezyk, A. A., *The Physics of fluid Suppl.*, 12(1969), 12 (II-77-86).
[12] Payne, R. B., *J. F. M.* 4(1958), 81—86.
[13] Kawaguti, M. & Jain, P., *J. Phys. Soc. Japan*, 21(1966), 2055—2062
[14] Son, J. S. & Hanratty, T. J., *J. F. M.*, 35(1969).
[15] Dennis, S. C. & Straniforth, A. N., *Lecture notes in physics*, 81(1971).
[16] Panikker, P. K. G. & Lavan, Z., *Journal of Computational Physics*, 18(1975), 41—65.
[17] Hiroyuki Honji & Sadatishi Taneda, *Journal of the Physical Society of Japan*, 27, 6(1969).
[18] Bryson, A. E., *Journal of applied Mech.*, 26, 4(1959).
[19] Mello, J. F., *J. A. S.*, 26 March, (1959)
[20] Sarpkaya, T. & Garrison, C. J., *Journal of applied Mech.*, 30, 1(1963).
[21] Yang, H. T. & Bar-Lev, *Journal of applied Mech.*, 43, 1(1976).
[22] Gerrad, J. H., AGARD Rep., 463(1963).
[23] Gerrad, J. H., *Phil. Trans. Roy. Soc.*, A261(1967), 137.
[24] Sarpkaya, T., *J. B. Engineering T. ASME*, 11(1968).
[25] Charin, A. J., *J. F. M.*, 57(1973), 785.
[26] Moore, D. W., *J. F. M.*, 63(1974), 225—235.
[27] Fink, P. T. & Soh, W. K., 10th Symp. Naval Hydrodynamics, Camb. Mass. (1974).
[28] Deffenbaugh, F. D. & Marshall, F. J., *AIAA J.*, 14, 7(1976), 908—913.
[29] Clements, R. R., AGARD Lecture Ser., 86(1977).
[30] Kunio Kuwahara, *Journal of the Physical Society of Japan*, 45, 1(1978).
[31] Sarpkaya, T. & Shoaff, R. L., *AIAA Journal*, 17, 11(1979).
[32] Milne-Thomson, L. M., Theoretical Hydrodynamics, The Macmillan Co. New York, 5th ed (1968).
[33] Rott, N., *Quart. Appl. Math.*, 13, pp. 444—451.
[34] Sears, W. R. & Tellionis, D. P., *SIAM Journal on applied mathematics*. 28, 1(1975).
[35] Telionis, D. P. & Tsahalis, D. T., 24th Internat. Astronautical Congress, Baku, 21, pp.
[36] Sarpkaya, T., AD A051781.
[37] White, F. M., Viscous fluid flow, McGraw-Hill Co. (1974).

DIFFICULTIES IN METHODS FOR SOLVING THE THREE-DIMENSIONAL FLOW IN TURBOMACHINERY

Chen Jingyi, and Liu Diankui
Institute of Engineering Thermophysics, Chinese Academy of Sciences
Submitted 26 November 1979

At present, most of the methods for solving the complete three-dimensional flow in turbomachinery have their foothold on Wu's theory of two families of stream-surfaces. In this paper the concept of the accuracy of the complete three-dimensional solution is clarified. The specification of boundary conditions is discussed for the subsonic case and a new suggestion for giving the boundary condition is presented. It is shown, that only if the boundary conditions of the two families of stream surfaces are fully compatible in the sense of rigorously satisfying the three-dimensional equations, would the complete three-dimensional flow solution converge to in an error less than any specified small value. In connection with the analysis of this paper some preliminary comparison and evaluation have been made with regard to the methods for solving complete three-dimensional flow in turbomachinery published since 1978.

Foreword

Advances have been made at home and abroad concerning the three-dimensional flow in turbomachinery; the so-called complete three-dimensional solution was introduced [1, 2]. However, this solution is still imperfect. For example, in calculating the internal flow field of a longitudinal-flow turbine, the result

in the study [1] presents a considerable warping stream surface, concluding the necessity for a complete three-dimensional solution. However, the results in the report [2] presents very little warpage of the s_1 stream surface with very little difference from the conventional two-dimensional solution. Likewise, the study [1] concludes that the accuracy of velocity convergence is limited to a numerical solution; the accuracy is different with different physical problems, as low as 6 percent in the examples cited in the manuscript. However, the report [2] does not have this limitation, arriving at an error of $3 \cdot 10^{-4}$ for the relative Mach number. Which one is correct? With reference to our work [3], these problems are analyzed here with relatively detailed comparison and discussion.

Discussions on the Method of Solution

The solution methods of [1], [2] and [3] are based on Professor Wu Zhonghua's theory of two families (s_1 and s_2) of stream surfaces. This theory serves to reduce the stream-surface concept of a three-dimensional problem to a two-dimensional problem of s_1 and s_2 stream surfaces. It can be proved that these two-dimensional problems are described by nonlinear elliptical type partial differential equations, under the premise of steady, non-viscous and subsonic flow. A complete three-dimensional solution aims at finding a three-dimensional field, which can satisfy a series of boundary problems at s_1 and s_2 stream surfaces. We introduce the following descriptions in the visualization: a certain blade-channel space is divided into a series of s_1 stream surfaces with a certain thickness of a stream slice, as well as for s_2 stream surfaces. To a two-dimensional problem, two geometric properties of shape and thickness are included in the solution of the boundary problem at a stationary stream surface. However, the three-dimensional problem involves solving a boundary value problem of two floating stream surfaces. The solution of each series of stream surfaces relates to another series of stream surfaces in how their geometric properties must be modified. With continuation of alternate superposition, the variables decrease continuously until complete motionless. In this case, the solution of two sets of the boundary value problems will coincide within a three-dimensional flow field; this is the final solution of a complete three-dimensional flow. Obviously, it does not share the same concept as the conventional two-dimensional boundary problem; it is entirely different as to the method of determining the solution accuracy.

According to the discussion above, the following conditions can be used to evaluate the accuracy of a complete three-dimensional solution [1, 3]:

$$\varepsilon_w = |W_{s1} - W_{s2}|_{max} < \varepsilon$$

In the equation, W_{s1} and $W_{\nu+1}$ are, respectively, the relative velocities found by solving the s_1 and s_2 stream surfaces at the same nodal point. The condition for evaluating the convergent accuracy adopted in the report [2] are:

$$\varepsilon_w = |W_{\nu+1} - W_\nu|_{max} < \varepsilon$$

In the equation, ν is the numbers of superpositionings and $W_\nu = (W_{s1} + W_{s2})/2$.

Obviously, convergence of W and $W_{\nu+1}$ does not indicate coincidence of the two sets (s_1 and s_2) of the two-dimensional solutions. The velocity field thus constructed does not satisfy the boundary value problems of either the s_1 or s_2 stream surface. The report [2] considers that this is the simultaneous satisfaction in the "average sense"; however, the "average" itself means the artificial weighting randomness. For example, we can take $W_\nu = A_1 W_{s_1} + A_2 W_{s_2}$ (A_1 and A_2 are the weighting constants taken randomly). It can be expected that according to the solution method in [2], the result of the same "convergence" is entirely different. Therefore, further discussion is needed on the accuracy of $3 \cdot 10^{-4}$ given in [2]. In [2], other series of the "averaging" method (there are continuity equations in addition to equations of motions) are adopted. This choice may blur the "individuality" of the s_1 and s_2 stream surfaces, so the amount of warpage of the s_1 stream surface finally computed is very small.

Suggestion for the Boundary Value Problem

In solving the boundary value problem, for the boundary condition and the actual physical problem to be consistent, in the traditional method of calculating the blade grid, the blade channel is extended to the upper and lower streams from approximately twice the grid distance to a point at infinite distance (i.e., the station). At this point, a homogeneous stream condition (Fig. 1) is given in order to automatically satisfy the equation of motion at the boundary. Thus, the physical problem itself can lead to a rational suggestion; however, the shape of the boundary stream and the distribution of stream slice thickness values are

difficult to be given in advance. For example, in calculation of s_2 stream surface, to the upper stream station of the axial-flow type compressor with internal gas-inlet cone and to the lower-stream station of centrifugal-type compressor, the randomness of extension of the meridian channel is very obvious. For a centrifugal turbine, in order to avoid supersonic difficulties while increasing the radius, the median channel in the lower stream must be changed to the expansion type. Besides, in the intermediate stage of a turbo-machine, as contrasted to a wind tunnel with a plane blade grid, often another row of blades is located with a very small gap in the front and rear of the other row of blades. Similarly, the boundary streamlines are difficult to extend toward the upper and lower streams. We calculated two similar centrifugal turbines; the only distinction is that the difference of x-coordinates (of the meridian-type lines outside the (K+1) station) is just 0.72 mm. If it is considered that the (K+1) station is a lower-stream extension station, the calculation indicates that the change is very obvious as caused by the turbine outlet flow field (K station). Figure 2 shows the velocity distribution as the s_2 flow surface divided in the middle.

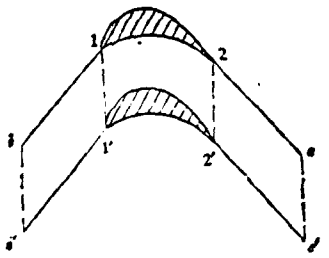

Fig. 1.

From [5], we introduced another solution method: the boundary is limited at the front or rear edge of the blade grid, or extended outward a very short station; the parameters at the boundary and the internal flow field are solved simultaneously. For an example of $\nabla^2\psi=0$ in a standard two-dimensional boundary problem (Fig. 3), if the same equidistant steps are taken in the x and y directions, and the boundary values are given at the upper and lower wall surfaces for the

subscripts $K=K_m$ and K_o, then all the internal node points (the upper-stream points with subscripts $j=j_o$, and the lower-stream points with subscripts $j=j_m$) in the solution region can be solved, respectively, by the following central, forward, and rearward differential forms:

$$\psi_{j-1,K} + \psi_{j+1,K} - 4\psi_{j,K} + \psi_{j,K-1} + \psi_{j,K+1} = 0$$
$$\psi_{j_o+2,K} - 2\psi_{j_o+1,K} - \psi_{j_o,K} + \psi_{j_o,K-1} + \psi_{j_o,K+1} = 0$$
$$\psi_{j_m-2,K} - 2\psi_{j_m-1,K} - \psi_{j_m,K} + \psi_{j_m,K-1} + \psi_{j_m,K+1} = 0$$

Altogether, $(K_m-K_o-1)x(j_m-j_o+1)$ linear independent equations are written. Hence, the solution includes the unknown function ψ of the same number of points of the internal node points, and upper- and lower-stream points.

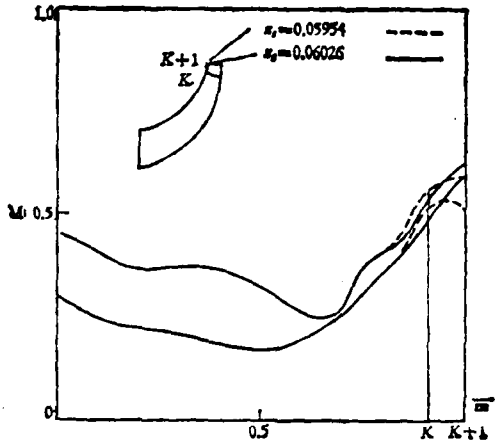

Fig. 2.

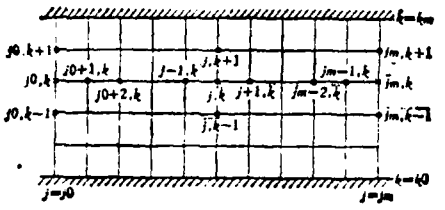

Fig. 3.

For a classic boundary problem, write $(K_m-K_o+1)x(j_m-j_o-1)$ equations according to the central differential form of the internal node points. In addition, the solution concerning only the internal node points is sought. For the points in the upper and lower streams, the boundary values are given according to some variation rule of the unknown function (the first category) or its derivative (the second category). In comparison, we can see that our solution method only gives the boundary condition corresponding to the variation rule of gas-flow parameters required by the equation of motion. It should be emphasized that the

above-mentioned differential form corresponds to the terminal-point condition of the constant second-order derivative when numerical calculations are made according to the sample-stripe function. As indicated by computations and practice, for a two-dimensional problem the suggestion of this boundary condition is still steady and convergent. Using a streamline iterative-substitution method on a computer, satisfactory accuracy as to the convergence of the entire-field streamlines (including the inlet and exit stations) can be obtained; for example, the absolute error is less than 10^{-6} mm and during the iterative-substitution solution, no effect on the perturbation of the initial value is shown. We believe that this suggestion method leads to a relatively rational physical problem because the equation is also satisfied at the boundary (although the central differential form cannot be used, the equation is not strictly satisfied). Moreover, the randomness of extending to the upper and lower streams can be avoided; therefore, this method is appropriate as a treatment method for boundary conditions in engineering calculations.

This solution method is used as the complete three-dimensional solution in the report [3]. In addition, to satisfy the periodic condition at the turbine exit, we extended one station from the turbine exit as the lower-stream boundary. The amount of adjustment of the circumferential-direction coordinate θ is expressed by $\Delta\theta$; the difference of velocities between the suction and pressure surfaces on the same revolving arc is expressed by ΔW. These two quantities are similar to those in [5]. We may adopt any method for solving roots to automatically find $\Delta\theta$, on a computer, by satisfying $\Delta W=0$. The report [3] makes detailed three-dimensional flow field computations for a rearward bent turbine. Figures 4 and 5 give, respectively, the ratios of streamline shapes and velocity distributions before and after the boundary adjustment of the upper and lower streams of the s_1 stream surface that is the closest to the external wall. Moreover, we are obliged to point out that as the periodic conditions are increasingly satisfied, the compatibility of boundary values of the s_1 and s_2 stream surfaces is also improved, thereby raising the accuracy of the three-dimensional flow-field solution from ε_W=10 percent before the adjustment to ε_W=3.5 percent.

We can see that in the computations in [2], no such adjustment is conducted. In the velocity fields given in Figs. 7, 8 and 9 in manuscript [2], the greater

the loading, the closer is the exit. So the s_2 stream surface does not remain close to the pressure surface of blades as seen in actual phenomenon; conversely, the s_2 stream surface is close to the suction surface of blades (the sliding coefficient μ of the turbine will be greater than 1).

We have to point out that the above-mentioned adjustment method often is not effective for centrifugal turbines with high loading at blades and constantly in separation flow condition as proven in experiments, especially for turbines with very few blades at the diametral-direction exit or with few blades. As indicated by computations, in this case the deviation amount of the streamline position at the lower-stream boundary is so large that it leads to too great a variation in streamline curvature at the exit station because of the non-viscous calculation, that the blade surface is required to be the stream surface. Thus, computations often result in overflow. This also explains the relationship between the physical phenomenon and the mathematical description; i.e., separation flows will exist in the neighborhood of the blade exit. When a flow function equation is adopted in seeking the solution, at stations with more frequent computations of the tail-edge region, the calculation results can satisfy the periodic condition; however, forced unloading will certainly lead to abrupt rises in pressure (often accompanying with violent oscillating motions) on the blade suction surface in the neighborhood of the blade exit. Actually, flows have been separated some time ago; therefore, the calculation result is still noncredible. Examples in [1] show smaller turbine loads (the difference of the relative Mach numbers of two blade surfaces at the exit cross-section); however, whether or not the calculations are consistent with the actual model depends on further proof.

Accuracy of Complete Three-Dimensional Solution

Actually, the accuracy of a complete three-dimensional solution is the extent of coincidence of two families of the two-dimensional boundary value problem. Therefore, the first factor affecting accuracy is the compatibility of the boundary condition. Moreover, since s_1 and s_2 are always solved separately; their differential equations do not approach the original equations with the same characteristics. For example, since the grid width ratios of s_1 and s_2 directions change greatly (in the case of diametral-flow-type turbine) from inlet to exit,

it is impossible to have the same interruption error. This is the reason why the accuracy is limited to a certain extent. The report [1] considers that the reason is the transformation of local grid; this is the effect of the second factor. The authors consider that the first factor may be the inherent reason.

First, let us view a very interesting numerical experiment: from example 2 of the report [3], when we adopt the solution method in which both inlet and exit stations are included in the solution range, and about 40 iterative substitutions are conducted at s_1 and s_2, the "best" accuracy thus obtained is

$$\varepsilon_W = |(W_{t_1} - W_{t_2}) / W_{t_1}|_{max} < 5\%.$$

The convergent accuracies of the streamline grid at θ and n directions are ε_{s_1,s_2}=0.3 mm. By further iterative substitutions, very slow divergence will occur (refer to Fig. 6 for the computation results with a different axial-flow turbine). However, if we fix the result of the 40th iterative substitution according to the streamline distribution at the inlet and exit stations (corresponding to the boundary condition of not strictly satisfying the motion equation) before iterative substitutions of s_1 and s_2, then the solution accuracies can be improved to $\varepsilon_W \approx 1$ percent and $\varepsilon_{s_1,s_2} \approx 0.04$ mm, and a very slow increase occurs with continuous iterative substitutions[a]. If we further fix the streamlines of the station inward from the inlet and exit, then the solution accuracy can be further improved to $\varepsilon_W \approx 0.5$ percent and $\varepsilon_{s_1,s_2} \approx 0.03$ mm (Fig. 7). Moreover, in the computations mentioned above, only when the maximum error of the streamline position occurs at the boundary cross section of the solution region, is the "limiting" accuracy of the solution obtained.

The computations mentioned above indicate an important effect of the boundary values. The reason why the fixed boundary can improve solution accuracy is because of the forced compatibility of the boundary conditions that are originally incompatible for s_1 and s_2, and the flow field in the vicinity of the boundary is made

---

a) The authors express their gratitude to Zhu Jungguo for his suggestions and assistances in the above-mentioned computations.

to adapt to the boundary condition, in addition to advantages due to solving the first-category boundary problem. However, since the boundary conditions are in forced compatibility, the improvement of accuracy is limited because at that time the boundary conditions do not strictly satisfy the three-dimensional equations. While the cross-section of the stationary boundary moves further inside, the further the boundary conditions are satisfied with regard to the three-dimensional equations, the higher is the compatibility. Hence, the process of improving accuracy mentioned above reappears once more at a higher level. Therefore, we consider that only when the given boundary conditions strictly satisfy the three-dimensional motion equations, are the conditions completely compatible. At that time, the accuracy of the three-dimensional flow-field solution can be randomly given. We also can deduce the following: if the solution region can be extended to an infinite distance toward the upper and lower streams, the flow fields there are uniform (in other words, automatically satisfying the three-dimensional motion equation), therefore the accuracy of the three-dimensional flow-field solution can be randomly given.

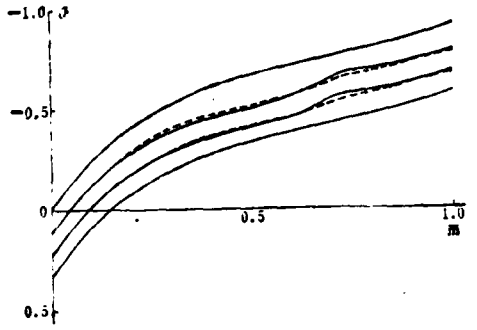

Fig. 4. ___ after adjustment; --- before adjustment.

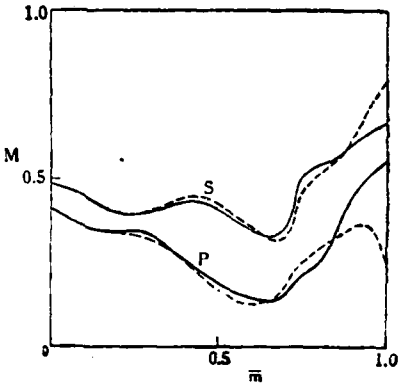

Fig. 5. ___ after adjustment; --- before adjustment.

We must explain that the discussion above is about the method of obtaining a three-dimensional solution by using the alternate iterative substitutions of two two-dimensional problems. This method is brief with well-defined concepts; however, there are new problems in the numerical solution. Usually in a two-dimensional boundary problem, the boundary value can be randomly given (even

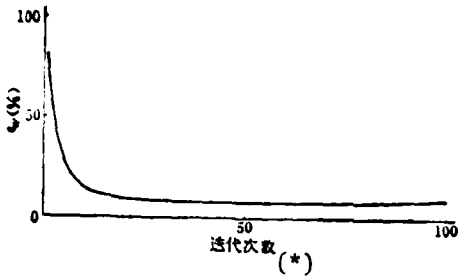

Fig. 6
Key: (*) Times of iterative substitution.

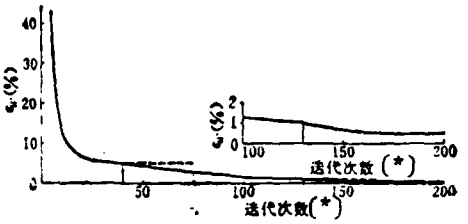

Fig. 7.
Key: (*) Times of iterative substitution.

though this does not necessarily satisfy the equation), to arrive at steady convergent solutions mathematically. However, in the three-dimensional solution, the requirement of compatibility of two two-dimensional problems is suggested; the distinction between two- and three-dimensional solutions is also manifested in the effect of grid density. For the same example, along the streamline direction the number of calculation stations is constant; however, while solving for motion equations, if different densities of grids are taken in the s_1 and s_2 directions, the accuracy is higher if we use a denser grid in a two-dimensional problem. The result is just the reverse in a three-dimensional problem. Moreover, we know that different equations can have determinate solutions only when the initial and boundary conditions are given simultaneously. This basic fact affects the accuracy of solutions by mutually iterative substitutions of differential equations; basically this is different from the solution of iterative substitution of algebraic equations. Previously, we discussed the accuracy of the iterative substitution solution of differential equations by using a procedure of reducing the number of dimensions. In recent years, some researchers used a procedure for varying the number of unknown functions to construct iterative substitution solutions of differential equations. At that time, similar limitations also exist in the solution accuracy; for example, in the solution method mentioned in [6], the errors can be convergent to less than 6 percent.

Conclusions

1. By using the alternate iterative substitution for two-dimensional problems of two families of stream surfaces, solutions of three-dimensional flow fields can be derived. This solution method introduces new mathematical problems that should be discussed. Our current understanding is as follows: the accuracy of solutions for complete three-dimensional flows is indicated by the extent of coincidence of solving two-dimensional problems of these two families of stream surfaces. This concept differs from the concept of accuracy in solving the conventional two-dimensional boundary problems. Only when the boundary conditions are completely compatible while strictly satisfying the three-dimensional equations, can the accuracies of solutions of three-dimensional flow fields be given randomly.

2. By simultaneously solving for boundary parameters and internal flow fields, in other words by using the solution method of given boundary values for the variation rule required by the motion equations, the physical problem becomes rational, relatively speaking.

3. In computations neglecting viscosity and separation, starting from satisfying the periodic conditions, it is necessary to make adjustments to the upper- and lower-stream boundaries; this is also advantageous in improving the solution accuracy of three-dimensional problems. However, for centrifugal turbines with high blade loads, a calculation method should be needed in a more realistic model of separate flow.

LITERATURE

1. Krimerman, Y., and Adler, D., The complete three-dimensional calculation of the compressible flow field in turbo-impellers, Journal of Mechanical Engineering Science, 20, 3 (1978).

2. Xin Xiaokang, Jiang Jinliang, and Zhu Shican, A method of random quasi-perpendicularly-intersecting planes in calculating three-dimensional flows of turbomachinery (II)--Calculation of three-dimensional flow of a warping S_1 stream surface, Lixue Xuebao [Journal of Mechanics], 1 (1979).

3. Liu Diankui, and Chen Jingyi, Three-dimensional flow solution method in turbomachinery--Iterative substitution method of "stream surface coordinates", Gongcheng Rewuli Xuebao [Journal of Engineering Thermophysics], 3 (1980).

4. Wu Zhonghua, A general theory of three-dimensional flow in subsonic and supersonic turbomachines of axial, radial, and mixed-flow types, NACA TN 2604 (1952).

5. Chen Jingyi, and Liu Diankui, General form and applications of turbomachinery motion equations along random curves, Yelun Jijian Qidong Reli Qisuan [Aerodynamic Calculation of Heat in Turbomachinery], Collection of papers at the design and experiment exchange conference (1976).

6. Dodge, P. R., Separated flow program, AD A-015707 (1975).

NUMERICAL COMPUTATION OF THE VISCOUS COMPRESSIBLE FLOW IN TURBOMACHINERY: (I) COMPUTATION OF AXISYMMETRICAL FLOW IN THE STATOR

Jiang Jinliang

Fudan University, Shanghai

Submitted 17 January 1979

Paper presents a numerical method for computing the various compressible steady laminar flows in turbomachinery. A numerical solution is obtained by iterative computation based on the enthalpy gradient equation, energy equation and entropy equation, expressed along arbitrary curved lines. This paper at first analyzes and discusses the computational method in a stationary coordinate system, and describes the method of axisymmetrical flow in the stator. As revealed by the computational examples, the characteristics of the method are brief procedures and high computation speed; therefore, the method may be widely applied in engineering design.

I. Foreword

Since Professor Wu Zhonghua presented the theory of stream surfaces [1] in 1952, the computational method of three-dimensional flow in turbomachinery has made rapid strides. At the present, efforts are underway to obtain the real three-dimensional flow solutions (for example, in [2]). However, all these computational methods consider fluid in flow channels as a nonviscous ideal fluid, which encounters mechanical loss due to its viscosity in the flow process; this loss can be

compensated by a loss factor obtained experimentally. Although this procedure avoids difficulties in calculating viscous flow, yet certain errors are introduced. In addition, this method cannot be used to compute problems of secondary flows in turbomachinery.

Later, Professor Wu derived a fundamental set of equations (in manuscript [3]) that a viscous compressible flow in turbomachinery must satisfy. In addition, he conducted detailed analyses of the function of viscous force and the physical significance of the viscous items. For other researchers, Patankar and Spalding [4] proposed adopting a propulsion integration method to calculate viscous flow in piping channels; Pratap and Majundar [5] adopted this method to calculate the viscous incompressible flow in a rectangle-shaped cross-section straight-pipe channel as the flow revolves around the axis of main-flow direction; and Ghia et al [6] adopted a polar coordinate system to calculate the viscous incompressible flow in a sector-shaped cross-section of a straight-pipe channel. These two above-mentioned pipe channels closely resemble turbomachinery channels; however, limited by the forms of equations they adopted and because during calculations, they neglected the second-order derivative items along the main-flow direction, the method only solves the problem of viscous flow in regular-shaped cross-section pipe channels. Until now, there has still been no solution in the calculation of viscous compressible flow in irregular-shaped variable cross-section bent pipe channels like turbomachinery channels.

This paper proposes a numerical computation method for viscous compressible steady laminar flow of an internal flow field. First, starting from the motion equation (Navier-Stokes equation) of viscous fluid, an enthalpy gradient equation is derived. Together with the energy equation and the entropy equation, the enthalpy gradient equation is used in making iterative computations. Through flux calibration, numerical solutions of viscous flow of the entire flow field can be obtained. As equations adopted in the paper are written in the derivative form along directions of three random curves, the method can be used to compute any shape bent pipe channels (including turbomachinery channels) of variable cross sections in solving the viscous compressible steady flow problems.

At first, the paper analyzes and discusses, with the assumption of a stationary system, to derive forms of equations; these equations are used to compute the viscous compressible symmetric flow of stationary blade rows in turbomachinery. The situation in these computations corresponds to considering the stationary blade rows as the number of blades approaches infinity and the blades become infinitesimally thin to be an extreme case. In this case, the three-dimensional flow field of the stationary blade rows can be considered as composed of an infinite number of S_2 flow surfaces, such as arc surfaces of blades. Therefore, there are the same distributions of flow parameters on each stream surface. In mathematical expression, this is an axisymmetric flow problem because flow is not related to θ; in mechanics, this can be approximately considered as making computations on the intermediate S_2 stream surface. In design problems (reverse problems), this flow model is continually adopted in making design calculations of blades. In checking problems (positive problems), on this basis the method can be used to conduct computations on the S_1 stream surface in order to obtain the numerical solutions of quasi-three-dimensional flow in stationary blade rows.

II. Fundamental Equations in Viscous Compressible Flow

1. The fluid is a compressible Newtonian fluid and satisfies Fourier's heat conduction flow law. 2. The fluid is an ideal gas. 3. The flow condition is steady. Therefore, the fundamental equations that a viscous compressible steady flow should satisfy are

$$\nabla \cdot (\rho \boldsymbol{v}) = 0 \tag{1}$$

$$(\boldsymbol{v} \cdot \nabla)\boldsymbol{v} = \boldsymbol{F} - \frac{1}{\rho}\nabla p + \frac{1}{\rho}\nabla \cdot [\tau] \tag{2}$$

$$\boldsymbol{v} \cdot \nabla h = Q - \frac{1}{\rho}\nabla \cdot \boldsymbol{q} + \frac{1}{\rho}\boldsymbol{v} \cdot \nabla p + \frac{1}{\rho}[\tau] \cdot \nabla \boldsymbol{v} \tag{3}$$

$$p = R\rho T \tag{4}$$

$$h = C_p T \tag{5}$$

In the equations, the unknowns are flow velocity v of the fluid, fluid density ρ, fluid pressure p, fluid temperature T, and enthalpy h of a unit mass of fluid.

The mass force F and amount of heat absorption Q are given; generally, these two quantities can be neglected. Also given are the gas constant R and the constant-pressure specific heat C_p. Under the hypothesis 1, the viscous stress tensor $[\tau]$ and amount of heat conduction q satisfy, respectively,

$$[\tau] = \mu\left\{\nabla v + (\nabla v)^{\prime} - \frac{2}{3}\nabla \cdot v[1]\right\} \tag{6}$$

$$q = -k\nabla T \tag{7}$$

In the equations, $(\nabla v)^T$ is the transposed tensor of tensor (∇v), [I] is the unit tensor, μ is the dynamic viscous coefficient of the fluid, and k is the heat conduction coefficient of the fluid. When the temperature variation is small, μ and k can be approximately considered as constants. However, C_p, μ and k also can be considered as known functions of temperature. By so doing, no difficulties will be incurred in the computation though the computation work will be increased. From the foregoing, equations (1) through (5) are closed; therefore, theoretically speaking, solutions can be obtained. However, in general situations it is quite difficult to solve these equations. Hence, before we conduct numerical computations these equations are first transformed.

In equation (1), its integration form can be used in this method.

$$\iint_A \rho v \cdot dA = G_0 \tag{8}$$

In the equation, A is the area of any cross section in the flow channel and G_0 is the given flow quantity.

To equation (2), by using the fundamental thermodynamic equation

$$TdS = dh - \frac{1}{\rho}dp \tag{9}$$

or its gradient form

$$T\nabla S = \nabla h - \frac{1}{\rho}\nabla p. \tag{10}$$

Combining equations (2) and (10), cancelling out the item $\frac{1}{\rho}\nabla p$ and neglecting the mass force F, we derive

$$\nabla h = T\nabla S + \frac{1}{\rho}\nabla \cdot [\tau] - (v \cdot \nabla)v \tag{11}$$

This equation indicates the relationship equation that enthalpy gradient should satisfy in a flow field; therefore, it is called enthalpy gradient equation, whose derivation is a feature of this method. One of the advantages is that the enthalpy gradient equation together with energy and entropy equations can be used to conduct alternate superimposition computation; S is entropy of the fluid and can be derived from integration of equation (9)

$$S = R\ln\frac{T^{\frac{\kappa}{\kappa-1}}}{p} \tag{12}$$

In the equation, x is the adiabatic index of the fluid.

To equation (3), the equation (10) is projected along the streamline direction, we get

$$\boldsymbol{v} \cdot T\nabla S = \boldsymbol{v} \cdot \nabla h - \frac{1}{\rho} \boldsymbol{v} \cdot \nabla p$$

Substituting equation (3) into the above equation, we get

$$\boldsymbol{v} \cdot T\nabla S = Q + \frac{k}{\rho} \nabla^2 T + \frac{1}{\rho} [\tau] \cdot \nabla \boldsymbol{v} \qquad (13)$$

that is

$$\frac{dS}{dl} = \frac{1}{vT} \left(Q + \frac{k}{\rho} \nabla^2 T + \frac{1}{\rho} [\tau] \cdot \nabla \boldsymbol{v} \right) \qquad (13')$$

In the equation, ℓ represents the distance coordinate along the spatial streamline, $dS/d\ell$ represents the variation rate of entropy along the streamline ℓ. Therefore, the equation is called the entropy equation.

Finally, look at the form of the enthalpy gradient equation (11) along the streamling direction

$$\boldsymbol{v} \cdot \nabla h = \boldsymbol{v} \cdot T\nabla S + \frac{1}{\rho} \boldsymbol{v} \cdot (\nabla \cdot [\tau]) - \boldsymbol{v} \cdot (\boldsymbol{v} \cdot \nabla) \boldsymbol{v}$$

By using equation (13) and vector computations, we get

$$\boldsymbol{v} \cdot \nabla \left(h + \frac{v^2}{2} \right) = Q + \frac{k}{\rho} \nabla^2 T + \frac{1}{\rho} \nabla \cdot ([\tau] \cdot \boldsymbol{v}). \qquad (14)$$

By introducing $h_0 = [h + (v^2/s)]$ which represents the total enthalpy (total energy) of a unit mass of fluid, equation (14) can be rewritten as

$$\frac{dh_0}{dl} = \frac{1}{v} \left[Q + \frac{k}{\rho} \nabla^2 T + \frac{1}{\rho} \nabla \cdot ([\tau] \cdot \boldsymbol{v}) \right] \qquad (14')$$

This equation indicates the variation rate of total energy of the fluid along a spatial streamline ℓ, therefore equation (14') is called the energy equation. We can see from the above that the energy equation is only the expression form of enthalpy gradient equation along the streamline direction.

Therefore, after transformation new equations are composed of equations (4), (5), (8), (11), (12), (13), and (14); equation (11) is a form resulting when only two directions are taken, except for the streamline directions. In the equations, the other unknowns are v, p, ρ, T, h, and S; therefore, the equations can be still considered as closed; they can be used to conduct numerical computation.

III. Equation Forms and Boundary Conditions in Turbomachinery

According to the flow characteristics of fluid in turbomachinery, a discussion can proceed by selecting a cylindrical surface coordinate system (r,θ, z); the z axis is coincident with the blade axis. To the axisymmetric flow considered in the paper, the partial derivative of all flow parameters to θ is 0. Therefore, the above-mentioned equations can be rewritten as the following forms:

(A) The entropy equation (11) can be rewritten as

$$\left.\begin{aligned}
\frac{\partial h}{\partial r} &= T\frac{\partial S}{\partial r} + \frac{\mu}{\rho}\left[\frac{4}{3}\frac{\partial^2 v_r}{\partial r^2} + \frac{4}{3}\frac{1}{r}\frac{\partial v_r}{\partial r} - \frac{4}{3}\frac{v_r}{r^2}\right. \\
&\quad \left. + \frac{\partial^2 v_r}{\partial z^2} + \frac{1}{3}\frac{\partial^2 v_z}{\partial r \partial z}\right] - \left[v_m\frac{dv_r}{dm} - \frac{v_\theta^2}{r}\right] \\
\frac{\partial \cdot}{\partial \theta} &= \frac{\mu r}{\rho}\left[\frac{\partial^2 v_\theta}{\partial r^2} + \frac{1}{r}\frac{\partial v_\theta}{\partial r} - \frac{v_\theta}{r^2} + \frac{\partial^2 v_\theta}{\partial z^2}\right] - v_m\frac{d(rv_\theta)}{dm}. \\
\frac{\partial h}{\partial z} &= T\frac{\partial S}{\partial z} + \frac{\mu}{\rho}\left[\frac{\partial^2 v_z}{\partial r^2} + \frac{1}{r}\frac{\partial v_z}{\partial r} + \frac{4}{3}\frac{\partial^2 v_z}{\partial z^2} + \frac{1}{3}\frac{1}{r}\frac{\partial v_r}{\partial z}\right. \\
&\quad \left. + \frac{1}{3}\frac{\partial^2 v_r}{\partial r \partial z}\right] - v_m\frac{dv_z}{dm}.
\end{aligned}\right\} \qquad (15)^*$$

In the equations, d/dm stands for the total derivative of flow parameters to the meridian streamline when the parameters vary along spatial streamlines; v_r, v_θ, and v_z are components of fluid velocity v in the cylindrical coordinate system

---

* For axisymmetric flow, $\frac{\partial h}{\partial \theta} = 0$. Therefore, the equations can satisfy the axisymmetric flow in a blade-less flow channel. As for the blade-row channel discussed at present, the item $\frac{\partial h}{\partial \theta}$ should be retained for the time being because of the existence of blade force.

(r, θ, z); and v_m is the projection of v on meridian plane. The following relationships are satisfied among v_r, v_θ and v_z:

$$v_r = v_m \sin\alpha \quad v_z = v_m \cos\alpha \quad v_\theta = v \sin\beta \quad v_m = v \cos\beta$$

In the equations, α is the meridian flow angle and β is the circumferential flow angle (see Fig. 1).

For any spatial curve q in the flow field, the direction derivative of enthalpy h along curve q is

$$\begin{aligned}\frac{dh}{dq} = {} & \frac{\partial h}{\partial r}\frac{dr}{dq} + \frac{\partial h}{\partial z}\frac{dz}{dq} + \frac{\partial h}{\partial \theta}\frac{d\theta}{dq} = T\frac{dS}{dq} + \left\{\frac{\mu}{\rho}\left[\frac{4}{3}\frac{\partial^2 V_r}{\partial r^2} + \frac{4}{3}\frac{1}{r}\frac{\partial V_r}{\partial r}\right.\right. \\ & \left. - \frac{4}{3}\frac{V_r}{r^2} + \frac{\partial^2 V_r}{\partial z^2} + \frac{1}{3}\frac{\partial^2 V_z}{\partial r \partial z}\right] - \left.\left[V_m \frac{dV_r}{dm} - \frac{V_\theta^2}{r}\right]\right\}\frac{dr}{dq} + \left\{\frac{\mu}{\rho}\left[\frac{\partial^2 V_z}{\partial r^2}\right.\right. \\ & + \frac{1}{r}\frac{\partial V_z}{\partial r} + \frac{4}{3}\frac{\partial^2 V_z}{\partial z^2} + \frac{1}{3}\frac{1}{r}\frac{\partial V_r}{\partial z} + \left.\left.\frac{1}{3}\frac{\partial^2 V_r}{\partial r \partial z}\right] - V_m \frac{dV_z}{dm}\right\}\frac{dz}{dq} \\ & + \left\{\frac{\mu r}{\rho}\left[\frac{\partial^2 V_\theta}{\partial r^2} + \frac{1}{r}\frac{\partial V_\theta}{\partial r} - \frac{V_\theta}{r^2} + \frac{\partial^2 V_\theta}{\partial z^2}\right] - V_m \frac{d(rV_\theta)}{dm}\right\}\frac{d\theta}{dq} \qquad (16)\end{aligned}$$

In the equation, q can be arbitrarily assumed as three random directions without a common plane in order to derive the equation satisfying the three directions. Usually, these three directions can be selected: first, it is the streamline direction; the enthalpy gradient equation along this direction is the energy equation (14) derived previously. Second, it is the θ direction. For axisymmetric flow, the equation along the θ direction is not necessary. Third, it is the spatial curve without a common plane of the streamline and the θ direction. This curve is called the computation-station line, briefly called the station line. When we compute on a middle S_2 stream surface, this station line must be situated on a middle S_2 stream surface; the projection curve of the station line on the meridian plane is called a meridian station line. Generally, a meridian station line can be taken as a straight line approximately perpendicular to the meridian streamline; this is the so-called quasi-normal line (Figs. 2, 3) in [7]. In this case, equation (16) can be rewritten as

$$\frac{dh}{dn} - T\frac{dS}{dn} + \left\{\frac{\mu}{\rho}\left[\frac{4}{3}\frac{\partial^2 V_r}{\partial r^2} + \frac{4}{3}\frac{1}{r}\frac{\partial V_r}{\partial r} - \frac{4}{3}\frac{V_r}{r^2} + \frac{\partial^2 V_r}{\partial z^2} + \frac{1}{3}\frac{\partial^2 V_z}{\partial r \partial z}\right] - \left[V_m\frac{dV_r}{dm} - \frac{V_\theta^2}{r}\right]\right\} \cdot \cos\varphi$$
$$+ \left\{\frac{\mu}{\rho}\left[\frac{\partial^2 V_z}{\partial r^2} + \frac{1}{r}\frac{\partial V_z}{\partial r} + \frac{4}{3}\frac{\partial^2 V_z}{\partial z^2} + \frac{1}{3}\frac{1}{r}\frac{\partial V_r}{\partial z} + \frac{1}{3}\frac{\partial^2 V_r}{\partial r \partial z}\right]\right.$$
$$\left. - V_m\frac{dV_z}{dm}\right\} \cdot \sin\varphi + \left\{\frac{\mu r}{\rho}\left[\frac{\partial^2 V_\theta}{\partial r^2} + \frac{1}{r}\frac{\partial V_\theta}{\partial r} - \frac{V_\theta}{r^2} + \frac{\partial^2 V_\theta}{\partial z^2}\right]\right.$$
$$\left. - V_m\frac{d(rV_\theta)}{dm}\right\}\frac{d\theta}{dn} \qquad (17)$$

In the equation, d/dn stands for the total derivative of flow parameters to the meridian station line n when the flow parameters vary along the spatial station line; ϕ is the angle of the meridian station line.

(B) The energy equation (14) can be rewritten as

$$\frac{dh_0}{dm} - \frac{1}{V_m}\left\{Q + \frac{k}{\rho}\left(\frac{\partial^2 T}{\partial r^2} + \frac{1}{r}\frac{\partial T}{\partial r} + \frac{\partial^2 T}{\partial z^2}\right) + \frac{\mu}{\rho}\left[V_r\left(\frac{4}{3}\frac{\partial^2 V_r}{\partial r^2} + \frac{4}{3}\frac{1}{r}\frac{\partial V_r}{\partial r}\right.\right.\right.$$
$$\left. - \frac{4}{3}\frac{V_r}{r^2} + \frac{\partial^2 V_r}{\partial z^2} + \frac{1}{3}\frac{\partial^2 V_z}{\partial r \partial z}\right) + V_\theta\left(\frac{\partial^2 V_\theta}{\partial r^2} + \frac{1}{r}\frac{\partial V_\theta}{\partial r} - \frac{V_\theta}{r^2} + \frac{\partial^2 V_\theta}{\partial z^2}\right)$$
$$\left. + V_z\left(\frac{\partial^2 V_z}{\partial r^2} + \frac{1}{r}\frac{\partial V_z}{\partial r} + \frac{4}{3}\frac{\partial^2 V_z}{\partial z^2} + \frac{1}{3}\frac{1}{r}\frac{\partial V_r}{\partial z} + \frac{1}{3}\frac{\partial^2 V_r}{\partial r \partial z}\right)\right.$$
$$+ 2\left(\frac{\partial V_r}{\partial r}\right)^2 + 2\left(\frac{V_r}{r}\right)^2 + 2\left(\frac{\partial V_z}{\partial z}\right)^2 + \left(\frac{\partial V_\theta}{\partial r} - \frac{V_\theta}{r}\right)^2 + \left(\frac{\partial V_\theta}{\partial z}\right)^2$$
$$\left.\left. + \left(\frac{\partial V_r}{\partial z} + \frac{\partial V_z}{\partial r}\right)^2 - \frac{2}{3}\left(\frac{\partial V_r}{\partial r} + \frac{V_r}{r} + \frac{\partial V_z}{\partial z}\right)^2\right]\right\} \qquad (18)$$

(C) The entropy equation can be rewritten as

$$\frac{dS}{dm} - \frac{1}{V_m T}\left\{Q + \frac{k}{\rho}\left(\frac{\partial^2 T}{\partial r^2} + \frac{1}{r}\frac{\partial T}{\partial r} + \frac{\partial^2 T}{\partial z^2}\right) + \frac{\mu}{\rho}\left[2\left(\frac{\partial V_r}{\partial r}\right)^2 + 2\left(\frac{V_r}{r}\right)^2\right.\right.$$
$$+ 2\left(\frac{\partial V_z}{\partial z}\right)^2 + \left(\frac{\partial V_\theta}{\partial r} - \frac{V_\theta}{r}\right)^2 + \left(\frac{\partial V_\theta}{\partial z}\right)^2 + \left(\frac{\partial V_r}{\partial z} + \frac{\partial V_z}{\partial r}\right)^2$$
$$\left.\left. - \frac{2}{3}\left(\frac{\partial V_r}{\partial r} + \frac{V_r}{r} + \frac{\partial V_z}{\partial z}\right)^2\right]\right\} \qquad (19)$$

All the three above-mentioned equations are rewritten as the derivative form of m and n along directions of random curves. If the right-hand items of the equations are predetermined, then these equations become simple differential equations. The problems become very simple; it is easy to make iterative computation. This is a characteristic of the method.

In order to compute the viscous compressible axisymmetric flow problems at stationary blade rows in turbomachinery, the following boundary conditions are required:

(1) In the blade-row flow channel, the velocity at the internal and external wall surfaces must be 0; i.e., $v_{wall}=0$. On the wall surface, there are two temperature situations: 1. the isothermal wall surface, i.e., given the temperature distribution situation on the wall surface; and 2. the adiabatic wall surface, i.e., the normal-direction derivative on the wall surface should be 0. According to the relationship equation (5) that satisfies the relationship between temperature and enthalpy, the boundary conditions of enthalpy can be suitably written out.

(2) When calculating flow in turbomachinery blade rows, in order to eliminate the effect and errors introduced by randomly selecting the boundary conditions at the exit, it is necessary to extend a distance toward the upper and lower streams from the inlet and outlet. In the region extending from the upper and lower streams, there is no function of blade force since this is the blade-less region. Therefore, in the middle equation of equations (15), let $\frac{\partial h}{\partial \theta}=0$ in order to get

$$\frac{d(rV_\theta)}{dm}=\frac{\mu r}{\rho V_m}\left(\frac{\partial^2 V_\theta}{\partial r^2}+\frac{1}{r}\frac{\partial V_\theta}{\partial r}-\frac{V_\theta}{r^2}+\frac{\partial^2 V_\theta}{\partial z^2}\right) \qquad (20)$$

This equation satisfies the circumferential-direction velocity V of gas flow in the extending region.

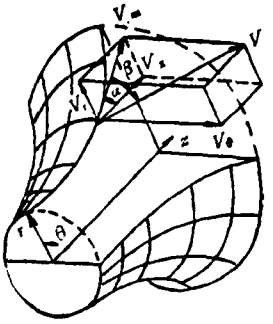

Fig. 1.

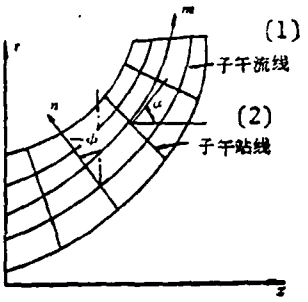

Fig. 2.
Key: (1) Meridian streamline; (2) Meridian station line.

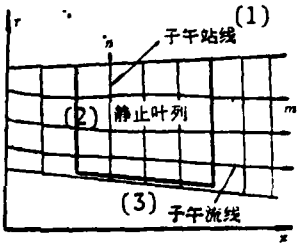

Fig. 3.
Key: (1) Meridian station line; (2) Stationary blade row; (3) Meridian streamline.

IV. Numerical Computation Method and Computation Examples

This paper adopts the streamline iterative method for the numerical computation. By taking examples of axisymmetric flow in the stationary blade rows in turbomachinery, the computation steps in the method are described as follows:

(1) At the middle S_2 stream surface (including the internal portion of stationary blade rows and the extending region toward the upper and lower streams), first several station lines q are selected. Then, according to some distribution

principle, assumed streamlines ℓ are marked. Thus, streamlines and station lines constitute a computation grid; on the grid points, assume the distribution situation of V_m, ρ, and T.

(2) The computation grid at the middle S_2 stream surface is projected onto a meridian plane to get a meridian grid composed of meridian streamline m and meridian station line n. Using numerical differentiation, we get the meridian flow angle α and meridian station line angle ϕ:

$$\alpha = \text{arc tg} \left.\frac{dr}{dz}\right|_{\text{along m}}$$

$$\varphi = \text{arc tg} \left.\frac{dz}{dr}\right|_{\text{along n}}$$

(3) In the internal region of the stationary blade rows, according to the shape of arc surface of the stationary blade rows, we then calculate V_θ and the circumferential-flow angle β:

$$V_\theta = V_m r \left.\frac{d\theta}{dm}\right|_{\text{along streamline } \ell} \tag{21}$$

$$\beta = \text{arc tg} \frac{V_\theta}{V_m} \tag{22}$$

For the reverse problem, V_θ can be computed from the selected stream types. Then the value of β can be computed from equation (22).

In the extending region, numerical integration and iterative computation on equation (20) can be conducted to obtain the value of V_θ. From equation (22), the value of β can be obtained.

(4) By using numerical differentiation, obtain the values of derivatives of flow parameters V_r, V_θ, V_z and T along the directions of meridian streamline m and meridian station line n. Then, use the characteristics of derivatives

$$\left.\begin{aligned} \frac{df}{dm} &= \frac{\partial f}{\partial r}\frac{dr}{dm} + \frac{\partial f}{\partial z}\frac{dz}{dm} \\ \frac{df}{dn} &= \frac{\partial f}{\partial r}\frac{dr}{dn} + \frac{\partial f}{\partial z}\frac{dz}{dn} \end{aligned}\right\} \tag{23}$$

In the equations, f stands for a certain flow parameter.

$$\frac{dr}{dm} = \sin\alpha \quad \frac{dz}{dm} = \cos\alpha$$
$$\frac{dr}{dn} = \cos\varphi \quad \frac{dz}{dn} = \sin\varphi$$

These are known quantities. Then the values of $\partial f/\partial r$ and $\partial f/\partial z$ can be obtained by solving the linear algebraic equations (23).

For second-order derivative values, similarly, by solving the linear algebraic equations

$$\left.\begin{aligned}
\frac{d^2f}{dm^2} &= \frac{\partial^2 f}{\partial r^2}\left(\frac{dr}{dm}\right)^2 + \left(\frac{\partial^2 f}{\partial r\partial z} + \frac{\partial^2 f}{\partial z\partial r}\right)\frac{dr}{dm}\frac{dz}{dm} + \frac{\partial^2 f}{\partial z^2}\left(\frac{dz}{dm}\right)^2 \\
&\quad + \frac{\partial f}{\partial r}\frac{d^2r}{dm^2} + \frac{\partial f}{\partial z}\frac{d^2z}{dm^2} \\
\frac{d^2f}{dn^2} &= \frac{\partial^2 f}{\partial r^2}\left(\frac{dr}{dn}\right)^2 + \left(\frac{\partial^2 f}{\partial r\partial z} + \frac{\partial^2 f}{\partial z\partial r}\right)\frac{dr}{dn}\frac{dz}{dn} + \frac{\partial^2 f}{\partial z^2}\left(\frac{dz}{dn}\right)^2 \\
&\quad + \frac{\partial f}{\partial r}\frac{d^2r}{dn^2} + \frac{\partial f}{\partial z}\frac{d^2z}{dn^2} \\
\frac{d^2f}{dmdn} &= \frac{\partial^2 f}{\partial r^2}\frac{dr}{dm}\frac{dr}{dn} + \frac{\partial^2 f}{\partial r\partial z}\frac{dr}{dm}\frac{dz}{dn} + \frac{\partial^2 f}{\partial z\partial r}\frac{dz}{dm}\frac{dr}{dn} \\
&\quad + \frac{\partial^2 f}{\partial z^2}\frac{dz}{dm}\frac{dz}{dn} + \frac{\partial f}{\partial r}\frac{d^2r}{dmdn} + \frac{\partial f}{\partial z}\frac{d^2z}{dmdn} \\
\frac{d^2f}{dndm} &= \frac{\partial^2 f}{\partial r^2}\frac{dr}{dn}\frac{dr}{dm} + \frac{\partial^2 f}{\partial r\partial z}\frac{dr}{dn}\frac{dz}{dm} + \frac{\partial^2 f}{\partial z\partial r}\frac{dz}{dn}\frac{dr}{dm} \\
&\quad + \frac{\partial^2 f}{\partial z^2}\frac{dz}{dn}\frac{dz}{dm} + \frac{\partial f}{\partial r}\frac{d^2r}{dndm} + \frac{\partial f}{\partial z}\frac{d^2z}{dndm}
\end{aligned}\right\} \qquad (24)$$

to obtain the second-order derivative values $\frac{\partial^2 f}{\partial r^2}$, $\frac{\partial^2 f}{\partial z^2}$, $\frac{\partial^2 f}{\partial r\partial z}$ and $\frac{\partial^2 f}{\partial z\partial r}$ of the flow parameters because theoretically, there must be

$$\frac{\partial^2 f}{\partial r\partial z} = \frac{\partial^2 f}{\partial z\partial r}$$

Therefore, we can take the average value as the value of $\frac{\partial^2 f}{\partial r\partial z}$ to be used in various equations.

(5) At every streamline (except the wall-surface streamlines), perform numerical integration on energy equation (18) and entropy equation (19). Moreover, determine the integration constant by using the values of total enthalpy and entropy at the inlet. Thus, the distribution of total enthalpy and entropy can be obtained for the entire flow field (except the wall surface).

(6) At each station line, perform numerical integration on the enthalpy gradient equation (17). In addition, using the boundary conditions of wall surface, the distribution of enthalpy h can be obtained. Then, using definition of total enthalpy and equations (12) and (4), we can get the values of v, p and ρ. An integration constant in numerical integration can be determined by using flow equation (8).

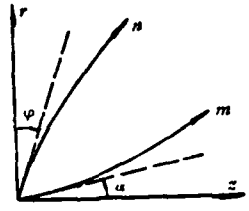

Fig. 4.

(7) According to the flow distribution principle determined in advance, using new streamline positions through reverse interpolation of flow and the relaxation factor of less than 1, we can get the new assumed positions of streamlines. Next, return to step 2 to make an iterative computation of the next cycle until the distance between the assumed position of the streamline and new streamline position can satisfy the requirement on accuracy. In this case, the computation result obtained is the numerical solution that we require.

In the above-mentioned computation steps, no detailed problems are mentioned regarding some numerical computations and the writing of programs. These details will be described and discussed thoroughly in another paper.

By using this method, computations of several flow channel arrangements were conducted. Here only a part of the computational results of stationary blade rows of a certain axial-flow-type turbine are plotted in Fig. 5. From the figure, we can see the effects on velocity and temperature resulting from viscosity.

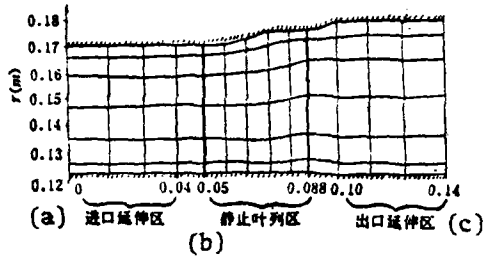

Fig. 5(a). Distributions of meridian streamlines and meridian station lines in stationary blade-row channel of axial-flow-type turbine.
Key: (a) Inlet extension region; (b) Stationary blade-row region; (c) Exit extension region.

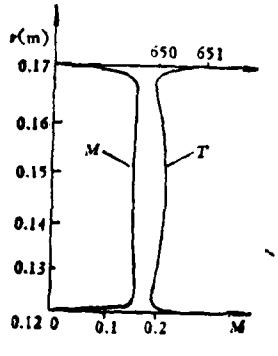

Fig. 5(b). Distributions of M and T at inlet cross-section.

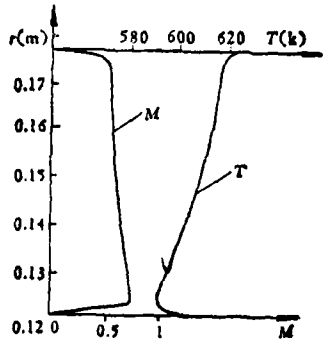

Fig. 5(c). Distributions of M and T at exit cross-section.

The characteristics of this method are simplicity, intelligibility, brief computation, and fast computation speed. From the above computation examples, 21 streamlines and 14 station lines are taken. Assuming the requirement that the

streamline error does not exceed 0.1 mm, the computation time on a 719 computer (125,000 operations a second) does not exceed five minutes (excluding the printout time). Moreover, the internal memory of the computer required does not have to be large. Therefore, this method can be widely applied in engineering design.

V. Conclusions

The paper proposes a new numerical computation method. Through iterative computations among enthalpy gradient equation, energy equation and entropy equation in the direction of a random curve, we can get numerical solutions of the viscous compressible steady laminar-flow problem of any random shape of variable cross-section bent pipe channel. Characteristics of the method include the establishment of fundamental equations of viscous flow in a grid of random curves. In addition, in iterative computations, these equations can be simplified into conventional differential equations, thus simplifying the computations.

The paper discusses the fundamental equations of a stationary coordinate system and the computation methods of axisymmetric flow problem. Moreover, numerical computations are conducted on axisymmetric flow in stationary blade rows in turbomachinery. The computational results indicate that the method is simple and feasible. In Part II, fundamental equations of viscous compressible flow of rotational coordinate system will be derived. In addition, numerical computations of axisymmetric flow of rotational blade rows in turbomachinery will be conducted.

LITERATURE

1. Wu Zhonghua, A general theory of three-dimensional flow in subsonic and supersonic turbomachines of axial, radial and mixed-flow types, NACA TN 2604 (1952).

2. Xin Xiaokang, Jiang Jinliang, and Zhu Shican, Lixue Xuebao [Journal of Mechanics], 1 (1979), 42-51.

3. Wu Zhonghua, The effect of viscous force and physical significance of viscous items in aerodynamic thermodynamics of stationary and motion coordinate systems, Jijian Gongcheng Xuebao [Journal of Mechanical Engineering], 13, 4 (1965).

4. Patankar, S. V., Spalding, D. B., A calculation procedure for heat, mass and momentum transfer in three-dimensional parabolic flows, International Journal of Heat and Mass Transfer, 15 (1972).

5. Pratap, V. S., Majumder, A. K., Spalding, D. B., Numerical computation of flow in rotating ducts, T. ASME. SI., 99, 1 (1977).

6. Ghia, V., Ghia, K. N., Staderus, C. J., Three-dimensional laminar incompressible flow in straight polar ducts, Computers and Fluids, 5, 4 (1977).

7. Katsanis T., Use of arbitrary quasi-orthogonals for calculating flow distribution in the meridian plane of a turbomachine, NASA TN D-2546 (1964).

A HIGH-SPEED INTERFEROGRAPH SYSTEM FOR INVESTIGATING FAST PHENOMENA

Xia Shengjie, Wang Chungkui, Fu Yushou, and Wu Baogen
Institute of Mechanics, Chinese Academy of Sciences
Submitted in March 1979

A system of high-speed interferograph for investigating the interaction of TEA CO_2 pulsed laser with matter and other fast flow phenomena has been constructed and applied successfully. Problems of the time synchronization and the optical match between high-speed camera and interferometer have been solved. We operated inversely an ordinary CW He-Ne laser to obtain a time-controllable pulsed light source. Several series of high-speed (microseconds) interference photographs of laser-matter interaction and the flow-field in supersonic wind-tunnel have been obtained. This technique may be used in other fast phenomena and flow-field visualization.

FOREWORD

In studying interactions of high-energy lasers and matter, complex physical processes occur. Appropriate means are required to observe and analyze these processes so many investigation techniques have been developed, from the areas of optics, electricity, spectrum, and X-rays [1, 2, 3]. The optical technique is the most widely used, because the technique involves one of the most direct observations of all approaches: it has been much refined in the study of phenomena in picoseconds, nanoseconds, and milliseconds.

To study the interaction of a 10.6-micron-wavelength pulsed laser and matter, we need to develop an optical method to investigate phenomena during this interaction. From the published reports, one- and two-dimensional studies in most experiments are conducted by simultaneous illumination and plasma growth with a stripe or frame-by-frame high-speed camera. In recent years, image-changing tube high-speed cameras (such as the Imacon series [4]) were used in picosecond and nanosecond studies on light sources of different wavelengths and relatively weak luminosity phenomena; the studies included stripe and frame-by-frame photographic recording. However, better recordings have not been obtained for phenomena of non-simultaneous illumination, weak luminosity, and disturbance of the medium near the interaction, such as air shock-wave due to the interaction, and intensive vaporization following laser irradiation on a target. In particular, few recordings of high-speed interference photographs are conducted with frame-by-frame continuity. Since high-speed interference photographs with frame-by-frame continuity makes possible the qualitative and quantitative analysis in time and space, we developed a high-speed interferograph device.

During its development, a continuous-wave 1 milliwatt He-Ne laser was used as the light source of an interference instrument, and the interaction of a dual-discharge CO_2 pulsed laser with matter was studied. A controllable type revolving lens scanning frame-by-frame superhigh-speed camera was used in making the photographs; a pulsed light source synchronized with the camera was also required. Although there are advantages with the He-Ne laser, such as good monochromaticity, small and flexible adjustment, and appropriate luminosity, there is still no pulsed type operation available for the He-Ne laser [1]. We applied its advantages and operational properties in suggesting a reverse-program operating plan to successfully modify the laser into a controllable pulsed type light source. We perfected this technique and obtained many highspeed interference photographs.

Technical Details of the Development

With a TEA CO_2 pulsed laser [5] with an output wavelength of 10.6 microns and approximately 4 joules of energy at atmospheric pressure, the output pulse width can be adjusted within a range of 1-100 microseconds. Different power densities of focusing light beams can be obtained with different lens focal lengths. The

laser can be used in studying physical phenomena occurring in laser-irradiated matter. Then a high-speed interference investigation system is used to record the photographs. See Fig. 1 for experimental layout

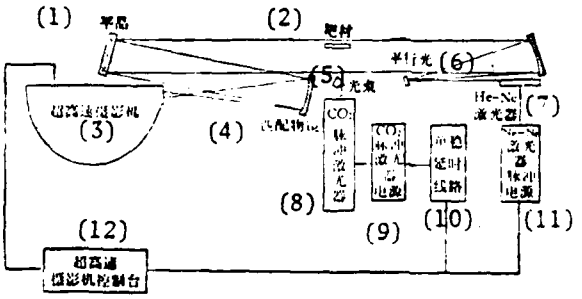

Fig. 1. Experimental layout.
Key: (1) Plane crystal; (2) Target; (3) Superhigh speed camera; (4) Matching objective lens; (5) Light beam; (6) Parallel light; (7) He-Ne laser; (8) CO_2 pulsed laser; (9) Power source of CO_2 pulsed laser; (10) Single steady delay circuit; (11) Pulsed power source of Ne-He laser; (12) Control platform of superhigh speed camera.

1. Fast processes are studied in the microsecond magnitude. For an accurate determination, first the phenomena in the study must be fully recorded within a short duration. All investigation segments should be time-synchronized. The shorter the duration, the more the synchronized segments, thus introducing more complications in synchronization.

2. Spatially speaking, for one- or two-dimensional signal recordings within a duration this short, we should solve the problems of light source luminosity and rate of phenomena recording.

3. The entire layout is in an environment of high-tension discharge puncturing the air, ionization and interference of high-energy electromagnetic waves. For example, the discharge voltage of a CO_2 pulsed laser is 40-50 kV and an initiating pulse of 40-50 kV is the output of high-speed camera control platform. These phenomena seriously affect normal operation of instruments and circuits, causing difficulties in experiments and studies. 51

4. A display device should be used to investigate non-instantaneous illumination, propagation of shock waves in a transparent medium, and the motion of a transparent vaporized matter. The light source of the display device should have good interference properties and meet the requirements of the highspeed camera. In other words, the light source should simultaneously exhibit interference and high luminosity properties in order to operate in a pulsed fashion, thus preventing overlapping exposure film.

5. The layout should be optically matched. During joint operation of the interference instrument and high-speed camera, there should be optical matching. Otherwise, the operation will fail.

Solution of Technical Problem Areas

1. Time synchronization

With the CO_2 pulsed laser used in the experiment, the output light pulse lasted 1 microsecond; the half width of the peak value is 100 nanoseconds while the laser is charged with a capacitor and the light emerges during the discharge from an initiating sphere gap. The time delay from the puncture of sphere gap to light emergence is measured approximately in microseconds. The lead time of the initiating signals as output of the controllable type high-speed camera is adjusted by the lead angle of the revolving lens. However, the lead time is only within one revolution of the revolving lens. Thus, the emergence of phenomena studied and the position of the revolving lens are synchronized. However, under special conditions, the phenomena studied may occur after the revolving lens gives an initiating signal and arrives at a working position of the time-delay rotation. If only the joint operation of the high-speed camera and the CO_2 pulsed laser is involved, their synchronization is simple, requiring only initiating the sphere gap by the camera. However, when another synchronization segment is required and this segment also occurs within a short duration, this kind of synchronization is relatively complex. The light source for the interference instrument is a He-Ne laser, which is small as the laser proper, and its power source and the laser have good interference properties. The He-Ne laser cannot operate in pulses [1]; the laser has a relatively long time delay from the occurrence of

the initiating signal to light emergence. The laser has relatively a long time deviation, about 20 milliseconds; this is the case when considerable excess pressure builds up when the initiating signal is to occur and its circuit is easily interfered with. To get accurate synchronization and a controllable pulsed light source, if the plan of igniting He-Ne laser involves an initiating signal, no time synchronization can be obtained. We suggested a plan of reverse-program operation by utilizing the operational properties of the He-Ne laser. When the applied current is weaker than the working current, the laser fails to glow. When the applied current exceeds the working current by a certain amount, the laser ignites but no light will emerge. If the laser is so arranged that the excess-current operation occurs only for a short duration, no light then occurs. After a synchronized signal is fed, and the excess current rapidly drops to the working-current level as controlled by an electron circuit, at that time, light emerges instantaneously and the current cutoff is delayed for a certain duration, this forms a single light pulse with short time deviation and a steady delay time. In the circuit, controllable silicon is used as the He-Ne laser switches. When the controllable silicon switches are closed, an excess current is adjusted in operation, and an external signal cuts off the controllable silicon switches, the He-Ne laser discharges, relying on the electric energy stored in the capacitor of filter circuit. The current index in the laser drops. At the working current, the laser liberates light. The light extinguishes when the current reaches a certain threshold value. Adopting this plan lowers the accuracy of time synchronization from more than 20 milliseconds down to 10 microseconds. Thus, the continuous-wave He-Ne laser is modified into a controllable single-pulse type light source with high accuracy in time synchronization; once the pulsed light source is matched with a revolving-lens scanning high-speed camera, the time synchronization between the two is carried out.

2. Luminosity of the light source

Light sources in high-speed photography involve a certain luminosity for normal film exposures. Visible light at 6328Å as the output of the He-Ne laser can produce an energy level of 10^{-2} erg/cm^2 [7] on a film sensitive to red light. If the interference elements of the (flat-crystal type laser) dislocation interferometer is a piece of plane crystal without coating films at both surfaces,

the light efficiency is only 8 percent. Efficiency this low is disadvantageous to high-speed photography. In this case, the minimum exposure time is calculated according to the following equation

$$\tau = \frac{SA}{P} \times 10^{-7} \quad \text{(sec)} \quad [7]$$

In the equation, τ is the exposure time in seconds; S is the sensitivity (ergs/cm^2) of the film; A is the illumination area in cm^2; and P is the power (watts) of the laser light source.

For example, an 1-milliwatt He-Ne laser is used as the light source and a plane-crystal interferometer without film coating is the main device. When the illumination area is ø10 millimeters, the minimum exposure time is:

$$\tau = 39.3 \cdot 10^{-6} \text{ sec}$$

To adopt to even higher exposure rates and to shorten the minimum exposure time, we adopted a plane-crystal interference element coated on both surfaces with adequate-reflectivity layers; light efficiency can be quintupled and a minimum exposure time of $7.8 \cdot 10^{-6}$ second can be realized. As proven by experience, wear occurs in the present optical system because of the presence of many optical elements. However, when Hangwei [transliteration]-II type film is used, a normal density can be obtained in the film for an exposure time longer than 5 microseconds. If a higher-power device is adopted, no doubt a shorter minimum exposure time can be obtained. For a 10-milliwatt device, a minimum exposure time of $7.8 \cdot 10^{-7}$ second can be obtained. If a watt level argon-ion laser is used, a minimum exposure time of 10^{-8} to 10^{-9} second can be obtained.

3. Restraint of interference

To screen disturbance from the high-energy electromagnetic waves, a measure of strong signal and high attenuation is adopted, and even the He-Ne laser has to be screened. Because when an intensity electric disturbance signal is applied to both terminals of an He-Ne laser with light emergence, the laser may be quenched, or the light intensity abruptly fades. In ways, interference is restrained.

4. Optical matching of high-speed interference photography

The high-speed camera and interferometer are two independent optical instruments. When they are operated together, the optical matching problem must be solved. The effective visual field of the interferometer should have an image of specified size formed by the camera. Thus, the visual field can be adequately utilized. This should require an attached lens to be set in the light channel to achieve optical matching between the high-speed camera and interferometer. A parallel light beam with a ϕ120 output diameter from the interferometer is easily adaptable to combined operation with the single-lens high-speed camera just by removing the objective lens of the camera and installing a larger-diameter (greater than the light-beam diameter) objective lens with proper focal length. Then the lens is adjusted to form a clear image of proper size on the film. Usually it is hard to find a large-diameter objective lens, but it can be replaced with a large-diameter concave spherical-surface reflective mirror with good results. Matching of the interferometer and a single-objective-lens high-speed camera can produce photographs of the growing plume of steam under laser irradiation, and high-speed interference photographs of supersonic shock waves in a wind tunnel; these can be examined to in the reports [6, 8]. Combined operation of the interferometer and the superhigh-speed camera with a revolving lens scanning frame-by-frame photographs is relatively complex. Since the optical system of a revolving lens scanning-type camera is an instrument with multi-lens combination, its field lens and light-alignment lens are strictly calibrated and fixed during design and manufacture. So matching between this optical system and the interferometer with large-diameter parallel light as its output demands a solution of the problem of light attachments in front of the field lens and light-alignment lens. Our conditions were as follows: the output of a plane-lens interferometer is a parallel light beam with 120 mm diameter; after image forming, the image on the film should have a 10 mm diameter; all instrument lenses should not cut off any portion of the light beam, that is, the dimensions of light spots at various lenses should be smaller than the effective lens apertures; the light spot at the light grating of the light-alignment lens should not be too large, otherwise the exposure time will be too long and the overlapping parts of the film exposure will be too many between two adjacent frames; and the dimensions of light spots at the mechanical shutter and revolving lens should be, respectively, smaller than the shutter diameter and the projection dimensions of the revolving lens

at its working position. Only when the above-mentioned conditions are met, can a complete visual field of the interferometer be achieved on the film. In order to design a large-diameter objective lens with proper focal length and appropriate arrangement of the light channel, in design a large-diameter reflective-type objective lens should be used. The objective lens is a spherical-surface reflective mirror with a 980 mm focal length, and the focus falls at the light axis 200 mm in front of the field lens (Fig. 2). The known quantities are as follows: the focal length of the field lens is 110 mm; the relative aperture diameter is 1:4.5; the focal length of the light-alignment lens is 56.3 mm; and the width of light grating of the light-alignment lens is 3.6 mm. In Fig. 2, A=53, B=159, and C=80. The calculations are as follows:

After focusing of the parallel-light-diameter concave lens M, the image is formed at 200 mm in front of the field lens. Through the field lens, an image is formed at a position having a distance of S' from the field lens

$$S'=Sf_{field}/(S-f_{field})=244.2 \text{ mm}$$

In the equation, S is 200 mm and f_{field} is the focal distance of the field lens.

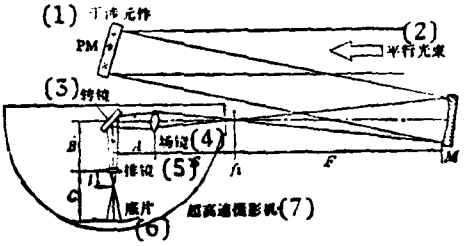

Fig. 2. Optical matching of interferometer and superhigh-speed revolving scanning type camera.
Key: (1) Interference element; (2) Parallel light beam; (3) Revolving lens; (4) Field lens; (5) Light-alignment lens; (6) Film; (7) Superhigh-speed camera.

The position from the light-alignment lens is $\ell=S'-A-B$.

The dimensions of light spots at various lenses and light grating are as follows:

(a) The dimensions of light spots at the field lens: $d_{field}=SD/F$

(b) The dimensions of light spots at the reflective mirror:

$$d_{field}=[(B+\ell)d_{field}]/(A+B+\ell)$$

(c) The dimensions of light spots at the light-alignment lens:

$$d_{field}= d_{field}/(A+B+\ell)$$

Because of the presence of light-alignment lens, the distance between the second focus and the light-alignment lens is closer than in the absence of the light-alignment lens. Actually,

$$\ell_{actual}=(-\ell f_{alignment})/(-\ell-f_{alignment})$$

We know from foregoing that the dimensions of image formed on the film are as follows:

$$d_{film}=[(C-\ell_{actual})d_{alignment}]/\ell_{actual}$$

Insert all data into the various equations, we obtain: the light spot at the field lens, ϕ24.5; the light spot at the lens surface, ϕ15.9; the light spot at the light-alignment lens, ϕ3.21; and the light spot at the film, ϕ9.4. All dimensions meet the requirements. The diameter of the concave reflective-type objective mirror is greater than 120 mm. After installation, the measured dimensions are in agreement with the calculated values.

With ordinary-light photography, the revolving-lens scanning-type optical system will have very small luminous flux of the instrument because of the presence of field lens, light-alignment lens, and front-mounted light grating. For normal exposures, the luminosity requirements on light source are quite high, particularly so in the superhigh-speed photography range. However, in the present layout, the field lens and light-alignment lens were coated with a transparency-enhancement

film, and in the light channel design no part of the light beam is cut off, so there is generally no loss. The light efficiency of the instrument is better and exposure time estimates are not effected by the instrument types. This means that superhigh-speed photography can be done with low-power (milliwatt level) light sources.

Calculations

After the above technical problem areas were solved, the layout was used to obtain a series of photographs showing interaction between laser and targets. Photograph 1 of the photograph section I shows the concentration of a TEA CO_2 pulsed laser beam on a focus, producing air puncturing and motion of shock waves. Photograph 1b in the same section shows the plane waves reflected by spherical shock waves from a spherical-surface reflective mirror. Each frame was exposed for 8 microseconds. The power of the pulsed He-Ne laser was 1.5 milliwatts. Photograph 2 of the same photograph section shows the puncturing and the jetting of high-energy vaporized matter from a solid target when irradiated with a pulsed CO_2 laser. The exposure time was 5.2 microseconds for each frame; the same light source was used. Thus far, the above-mentioned light source has been used to take high-speed interference photographs of 1.3 microseconds of exposure for each frame. These recordings no doubt can provide qualitative and quantitative evidence of the interaction of lasers and matter.

In addition, the experimental results proved that this investigation technique can be used to show more displays of high-speed flow fields, like laser wind tunnel, explosion, combustion, and plasma. Photograph 3 of the photography section I shows an investigation, using this installation of a light-cavity flow field of an aerodynamic laser. We can determine the effect on quality of output light beam by the position of shock waves produced at the throat channel. Photograph 4 of the photography section I shows the flow-field photograph near a model placed in a M 2.5 wind tunnel. The two above-mentioned photographs were taken by using an 1-milliwatt He-Ne laser with continuous wave output as the light source; each frame exposure is 0.5 and 1 millisecond, respectively.

LITERATURE

1. John, F. Ready, Effects of High-power Laser Radiation, (1971).

2. Helmut, J. Schwarz, Laser Interaction and Related Plasma Phenomena, (1971).

3. Lieber, A. J., et al, 11th H. S. P., 1974.

4. Huston, A. E., High-speed photography and photonic recording, J. Phys. E: Sci. Instrum., 11 (1978).

5. Fu, Yushou, Applications of double discharge CO_2 laser, Jiguang [Laser], 3, 6 (1976).

6. Liu, Jianbang, and Xia,Shengjie, Applications of plane-crystal type laser dislocation interferometer in measuring flow fields, Lixue Xuebao [Journal of Mechanics], 4 (1978).

7. Holland, T. E., Applied Optics and Optical Engineering, Vol. IV, Part 1, p 211.

8. Zhou,Guangdi, Xia, Shengjie, et al, Images and growth of steam plume with laser irradiation, Jiguang [Laser], 5, 5-6 (1978), 21.

9. Lunn, G., A general survey of high-speed photographic technique, J. Smpte, 71, 12 (1962).

STATISTICAL SIMULATION OF THE AERODYNAMIC BEHAVIOR OF THE TRANSITIONAL REGION OF FLOW PAST COMBINED BODIES OF REVOLUTION AT ARBITRARY ANGLES OF ATTACK

Wu Zhenyu, Li Fenglin, and Lin Baozhen

Unit #89956, Chinese People's Liberatuion Army (Wu), Computer Center of the Chinese Academy of Sciences (Li), and Chinese Academy of Space Technology (Lin)

Submitted in March 1980

In this paper, we set up a three-dimensional statistical simulation model for the problem of rarefied gas hypersonic flow past combined bodies of revolution with an angle of attack. In order to improve the efficiency of the simulation and to expand the simulation region, we adopt a special weighting technique and reduced collision model. A series of calculation has been executed on 013 Computer and the results are very satisfactory.

I. Foreword

Studies of aerodynamic properties in rarefied gases are decidedly important for space flight vehicles (extended flights), such as meteorological satellites, manned and other spacecraft [1]. In recent decades, researchers studying rarefied gas aerodynamics have persisted in trying to solve the Boltzmann equation, yet up to now no important breakthrough was forthcoming. For urgent and practical problems, they rely only on experiments and engineering methods. However, the statistical simulation method developed by Bird can provide almost all aerodynamic

data [2, 3] for flight vehicles over the entire transitional region. Relying on Bird's contribution [2] and the report [4], the authors established a statistical model of combined bodies of revolution for three-dimensioanl circulation flow; a series of calculations were made for a short conical frustum at its base of the spherical platform, to derive the pressure coefficient c_p, friction coefficient c_f, heat transfer coefficient st, coefficient of axial force c_A, coefficient of normal force c_N, moment coefficient c_m, pressure center position x_{cp}, and other parameters. For better simulation efficiency and longer computation range, a method of simulated molecular weighting is introduced based on Bird's approach [2]. The computational results are in general agreement with the experimental results. This paper briefly introduces some computational results.

II. Description of Method

A statistical simulation method is actually a gas flow process simulated by a computer; a space region is marked out and referred to as a flow field. This paper adopts a cylinder-shaped flow field; an object is placed in the central portion of the flow field; the object's symmetrical axis is coincident with that of the flow field. The incoming flow is placed in the XY plane. From these assumptions, it is sufficient to only simulate one half of the space (see Fig. 1). The study [4] describes the grid division, simulation of the initial position of molecules, determination of velocity, and methods of supplementing molecules at the inlet of the flow field. The simplification and treatment methods of collisions are borrowed from the report [2]. The molecules exhibit a mirror-surface reflection to the symmetrical plane (Z=0). The reflection model on the object surface is cited from the studies [2, 3].

To extend the simulation range and for better simulation efficiency, this paper adopts a weighting technique, by assigning different weights to simulation molecules of different parts of the flow field. In other words, weights represent actual gas molecules in different numbers. The method used in the paper consists of assigning weights along the diametral direction of the flow field. Let $r_{i,j,k}$ stand coordinates at the diametral direction of grid nodal points with subscripts (i, j, k). Because of different weights, when a simulated molecule enters another

grid from a grid, the molecule may disappear, continuously exist, or divide into several simulated molecules. For an example, when a simulated molecule enters another grid from a grid, the molecule may disappear, continuously exist, or divide into several simulated molecules. For an example, when a simulated molecule enters another grid with subscripts (i, j, k+1) from a grid (i, j, k), should we use a random number to determine whether or not the molecule continuously exists? When

$$R_i \leqslant \frac{2r_{i,j,k}+1}{2r_{i,j,k+1}+1}$$

the molecule exists continuously. Otherwise, the molecule disappears. In the equation, R_f is a random number with a uniform distribution in (0-1) regions. If a simulated molecule enters another grid with subscripts (i, j, k+1) from a grid (i, j, k), then a simulated molecule may divide into several molecules; the integer-number part of the expression equation $(2r_{i,j,k+1}+1)/(2r_{i,j,k}+1)$ shows the number of molecules after dividing. If the part following the decimal point is greater or equal to the random number R_i, to the number of daughter molecules is added 1; otherwise, no addition is made. For the situation of several daughter molecules, it is necessary to artificially handle the molecule position and velocity in order to have a slight difference between the velocities of daughter molecules and to ensure that any point in space can be occupied by one simulated molecule at most. Thus, compute the collisions between molecules and trace the variation in position and velocity of each simulated molecule. The recordings and their proper treatment can lead to various parameters representing aerodynamic properties.

III. Analysis of Results

By using the above-described method, in the paper a series of computations of a combined body of revolution having circulation flow with angle of attack is made. The exterior of the combined body of revolution is shown in Fig. 2. The variation range of incoming-flow parameters is 16-22 (s is the ratio of the incoming-flow velocity and the thermodynamic velocity of the molecules); the ratio of wall temperature and total temperature $\hat{T}_W$=0.1 to 0.13; the angle of attack α=0 to 20°. Computations were conducted on a Chinese-made 013 Computer; the operating speed of the floating point mode of the computer is 2 million times per second, and its internal memory can hold 130,000 words. The number of initial

molecules, without weighting, are $3\cdot10^3$ to 10^4. The dimensionless length of time step is $\Delta\tilde{t}$ at 0.01-0.05 ($\Delta\tilde{t}=\Delta t\cdot c_{m\infty}/\lambda_\infty$; here Δt, $c_{m\infty}$ and λ_∞ represent, respectively, the length of time segment, thermodynamic velocity of molecules in incoming flow, and the average collision freedom). In order to eliminate as much as possible the influence of non-equilibrium effect, sampling begins after a 40-60$\Delta\tilde{t}$ time interval; the sampling period is 40-80$\Delta\tilde{t}$. At zero angle of attack, there are two regions along the direction of the argument; there are divided into three or four regions when the angle of attack is not equal to zero. When the weighting technique is used, the number of initial molecules is $1.5\cdot10^3$-$5\cdot10^3$.

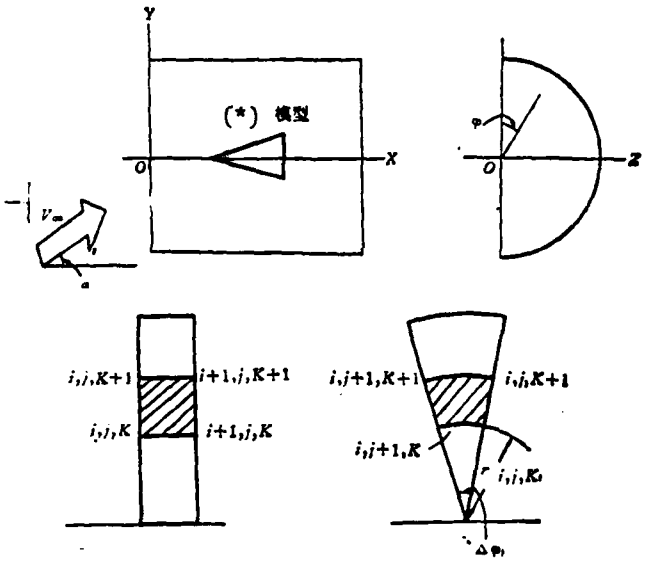

Fig. 1. Division of three-dimensional flow field and grid.
Key: (*) Model.

Figure 2 shows a velocity diagram without weighting; data are obtained from the first and fourth region in the direction of the argument; these can be approximately considered as the windward and leeward surfaces; the length of line segments stands for the magnitude of velocities; directions are represented by arrows. Since the velocity component at Z direction is neglected, the diagram gives $\sqrt{V_x^2+V_y^2}$ as the actual figure. The velocity diagram shows some

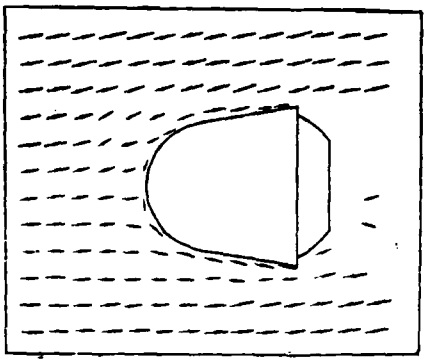

Fig. 2. Velocity spectrum of $(V_X^2+V_Y^2)^{1/2}$
$K_{n_{D_\infty}} = 0.167, \quad S = 20$
$\bar{T}_W = 0.1, \quad \alpha = 10°$

flow details. First, near the stationary point, the magnitude and direction of velocity have changed apparently. Secondly, the disturbance at the windward surface of the object is greater than the leeward surface. Lastly, from an analysis of the flow field, we can see that when the angle of attack α is increased, the diametral-direction length of the flow field also correspondingly increases in order to compare two reflection models from the wall surface and to calculate the situation of two sets of zero angle of attack, Fig. 3 gives the comparison between the calculated drag coefficients and experimental results [5]. Basically, the calculated data are in agreement with the experimental results. There are little differences in effects between two models; this is possibly because the incoming velocity is quite high.

Variations of aerodynamic coefficients c_A, c_N, and c_m with the angle of attack α are given in Fig. 4. α is 0°, 5°, 10°, and 20°. In these figures, when α=0°, the sampling period is $40\Delta\tilde{t}$; in other cases, the sampling period is $80\Delta\tilde{t}$. The darkened symbol when α=10° represents the computational result without weighting. It is apparent that the weighting method is successful. From the figure, we also can see linear variations of c_N and c_m with the angle of attack; the result is completely identical with the conclusion obtained from the rarefied-gas experiment when the angle of attack is small.

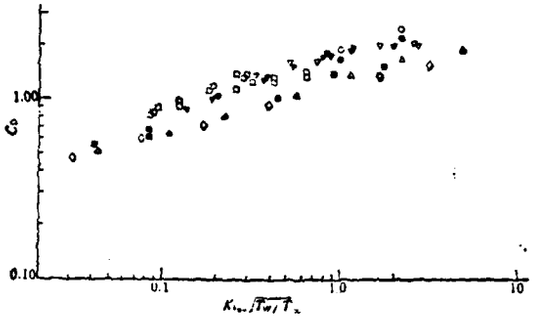

(a) (b) (c)

符号		设备	M_∞	半锥角
□		AFDC Tunnel "L"	0.4, 10	15°
■		GE Shock Tunnel	21.7, 24.2	15°
▲		GE Shock Tunnel	21.7, 24.2	6°
◇		GE Shock Tunnel	21.7, 24.2	6° (钝)(g)
▽		VKL Free Jet	8.4	13.5°
▼	(d)	(e)	11.5	13.5°
○	本文	[2]的反射模型	−22	10°
● (d)	本文	[3]的反射模型(f)	−22	10°

Fig. 3. Comparison between theoretical values and experimental values (drag coefficient c_D).
Key: (a) Symbols; (b) Layout; (c) Semi-conical angle; (d) This paper; (e) Reflection model in [2]; (f) Reflection model in [3]; (g) (Obtuse).

This paper derives an isothermal-curve diagram (Fig. 5) concerning temperatures; the curves connect various points of same temperature in the flow field. Since the wall temperature is relatively low, at the nose portion a high-temperature region is formed; the curve is generally symmetrically distributed near the stationary point.

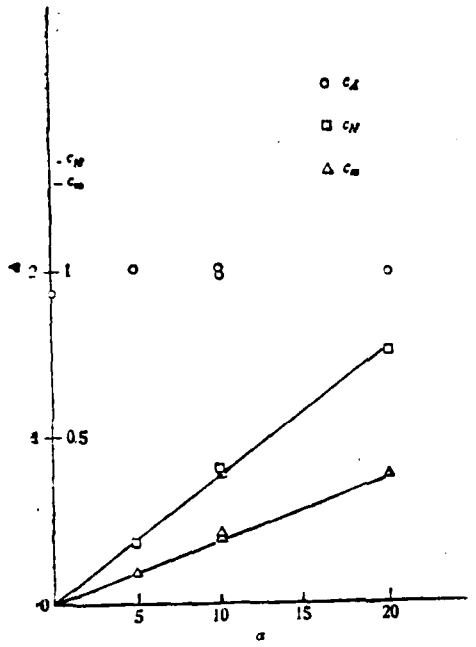

Fig. 4. Variations of c_A, c_N and c_m with α.

o c_A □ c_N △ c_m

IV. Conclusions

In the paper, a series of computations are conducted concerning rarefied-gas circulation flow. As indicated by results, a three-dimensional statistical model is established on the basis of two-dimensional and symmetrical circulation flow calculations as reported by the studies [2-4]; both the three-dimensional statistical model and the adopted weighting method are successful.

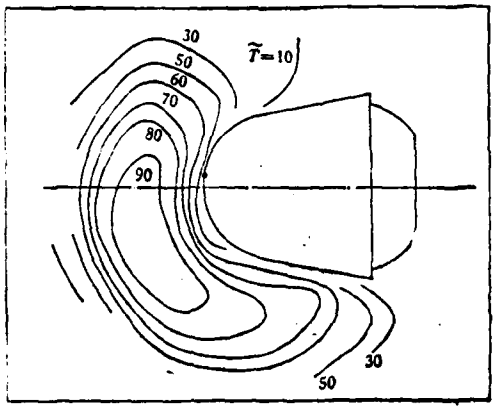

Fig. 5. Isothermal curves diagram

$\varepsilon = 20 \quad \tilde{T}_w = 0.1 \quad \alpha = 20° \quad \tilde{T} = T/T_\infty$

LITERATURE

1. Wu, Zhengyu, Qidong Yanjiu He Fazhan [Aerodynamic Studies and Development], 2 (1979).

2. Bird, G. A., Molecular Gas Dynamics (1976).

3. Takagi, M., Univ. Tokyo Report, No 473 (1971).

4. Li Fenglin, Wu Zhenyu, and Zhen Guoguang, Jisuan Shuxue [Computational Mathematics], 3 (1978).

5. Geiger, R. E., AIAA Paper (1969), 69-711.


FILMED
7-8